Boron-doped Sucrose Carbons for Supercapacitor Electrode: Artificial Neural Network-Based Modelling Approach

Amirhossein Fallah

Submitted to the
Institute of Graduate Studies and Research
in partial fulfillment of the requirements for the degree of

Doctor of Philosophy
in
Chemistry

Eastern Mediterranean University
September 2020
Gazimağusa, North Cyprus

Approval of the Institute of Graduate Studies and Research

_____
Prof. Dr. Ali Hakan Ulusoy
Director

I certify that this thesis satisfies all the requirements as a thesis for the degree of Doctor of Philosophy in Chemistry.

_____
Prof. Dr. İzzet Sakallı
Chair, Department of Chemistry

We certify that we have read this thesis and that in our opinion it is fully adequate in scope and quality as a thesis for the degree of Doctor of Philosophy in Chemistry.

_____
Prof. Dr. Mustafa Gazi
Supervisor

Examining Committee

1. Prof. Dr. Murat Ateş   _____

2. Prof. Dr. Mustafa Gazi   _____

3. Prof. Dr. Bahire Filiz Şenkal   _____

4. Prof. Dr. Elvan Yılmaz   _____

5. Assoc. Prof. Dr. Hayrettin Ozan Gülcan   _____

ABSTRACT

Here, a simple yet efficient and economic strategy was demonstrated for the production of multiporous boric acid-doped sucrose carbon (B_x–pC) for supercapacitor application. The electrochemical performance was established through cyclic voltammetry and galvanostatic charge/discharge tests. B_x–pC samples were characterized by X-ray diffraction, scanning electron microscope, Raman spectroscopy and nitrogen adsorption/desorption at -196 °C. The results reveal that the optimum boron dopant is 2 wt.%; and B_2–pC containing 2 wt.% boron exhibited honeycomb-like porous structure (2.88 nm) and a high specific surface area of 1298.9 m^2g^{-1}. The B_2–pC based symmetric supercapacitor delivered a remarkable energy density of ~56 Wh kg^{-1}, a high power density of 1300 W kg^{-1} and superior capacitance of 239 F g^{-1} at 1 A g^{-1} in 1 M H_2SO_4 electrolyte. To establish the complex relationships between the electrode structure, active operating conditions and electrochemical performance of the supercapacitor, an artificial neural network (ANN) methodology was utilized herein. After several random runs, the ANN maintained satisfactory predictive performance with an average error rate of ~1.06% and desirability function of 0.93 which is closer to 1.0.

Keywords: supercapacitor performance; sucrose-based porous carbons; artificial neural network optimization; electrochemical analysis.

ÖZ

Burada, süperkapasitör uygulaması için çok gözenekli borik asit katkılı sükroz karbon (B_x–pC) üretimi için basit ama etkili ve aynı zamanda da ekonomik olan bir strateji gösterildi. Elektrokimyasal performans, döngüsel voltametri ve galvanostatik şarj / deşarj testleri ile belirlenmiştir. Bx – pC numuneleri, X-ışını kırınımı, taramalı elektron mikroskobu, Raman spektroskopisi ve - 196 ° C'de nitrojen adsorpsiyonu / desorpsiyonu yöntemleri kullanılarak karakterize edildi. Sonuçlar, optimum bor katkı maddesi miktarının ağırlıkça %2 olduğunu göstermiş; ve ağırlıkça %2 bor içeren B_2–pC numunesinin de bal peteği benzeri gözenekli yapısı (2.88 nm) olduğunu ve 1298.9 m^2g^{-1} gibi yüksek bir özgül yüzey alanına sahip olduğunu sergilemiştir. B_2–pC tabanlı simetrik süper kapasitör, ~56 Wh kg^{-1} gibi dikkate değer bir enerji yoğunluğu, 1300 W kg^{-1} değerinde yüksek güç yoğunluğu ve 1 M H_2SO_4 elektrolitinde 1 A g^{-1}' de 239 F g^{-1} değerinde üstün bir kapasite sağladı. Elektrot yapısı, aktif çalışma koşulları ve süper kapasitörün elektrokimyasal performansı arasındaki karmaşık ilişkileri kurmak için, burada bir yapay sinir ağı (YSA) metodolojisi kullanılmıştır. Birkaç rastgele çalışmanın ardından, YSA ortalama hata oranı ~% 1.06 ve arzu edilirlik fonksiyonu 1.0'a yakın olan 0.93'lük tatmin edici tahmin performansını sürdürmüştür.

Anahtar kelimeler: süper kapasitör performansı; sükroz esaslı gözenekli karbonlar; yapay sinir ağı optimizasyonu; elektrokimyasal anali.

DEDICATION

This thesis is dedicated especially to

My lovely wife

Foroogh Khosravi

My dearest and respected parents

Aliakbar Fallah and Marzieh Kavyanirad

and

My siblings

ACKNOWLEDGMENT

First and foremost, I would like to thank Almighty God for blessing me with the ability, will, and opportunity to complete this thesis and my study.

My utmost gratitude goes to my supervisor Prof. Mustafa Gazi for giving me the opportunity to undertake this research. Thank you for the patience and advice.

To Assoc. Prof. Dr. Hayrettin Ozan Gulcan, thank you for the constant advice, helpful suggestions, fruitful discussions, and interesting experiences. You are an inspiration and a continuous source of knowledge.

My sincere appreciation also goes to Assoc. Prof. Dr. Akeem Oladipo for the helpful advices, discussions and guidance in helping me to complete my work and this thesis. Thank you to my colleagues and friends who always support me during my Ph.D.
To my lovely wife and my dearest family, I would like to express my very special gratitude for the prayers and words of encouragement. Thank you for standing by me, bringing cheer and happiness to my life.

TABLE OF CONTENTS

LIST OF TABLES

LIST OF FIGURES

Chapter 1

INTRODUCTION

1.1 Background

One of the greatest topics to pursued due to decrease the dependence to fossil fuels which cause climate change and environmental pollution are renewable energy resources. Energy resources during the centuries has changed from the Earth's natural resources such as plants to coal, oil, and nowadays biomasses. Noteworthy, the combustion of fossil fuels resulted to release environmental pollutions specially CH_4 and CO_2 known as greenhouse gases. From this perspective, production of green energy and energy storage are demanded due to protect environment from the pollutions and greenhouse gases and also replacing with fossil fuels [1][3]. Electrochemical capacitors, also called supercapacitors, have received tremendous attention as promising energy storage device in portable electric devices, emergency power back up, and electric vehicles due to their excellent advantages include ultrahigh energy and power density, long cycle life, and outstanding pulse charge-discharge performance [4][6].

Figure 1.1 shows the Ragone plot, power density against energy density, for some common energy storage systems. In this plot supercapacitors shows higher power density and energy density comparing to lithium batteries and conventional capacitors respectively. Although the energy density of supercapacitors is higher than conventional capacitors but is remarkably less than batteries.
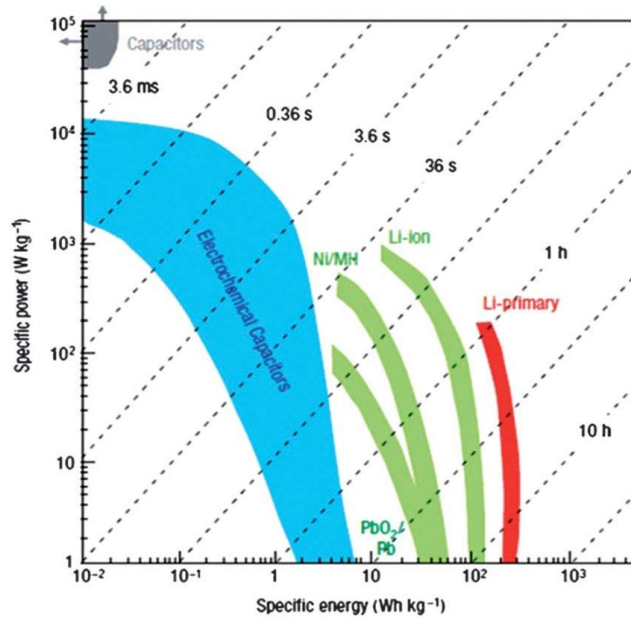
Figure 1.1: Ragone plot, demonstrating the specific energy versus specific power for different devices used as energy storage [1]

Supercapacitors mainly are grouped into an electrochemical double-layer capacitors (EDLC) and pseudocapacitor. Based on their energy storage mechanism, EDCLs store energy through reversible and fast electrostatic adsorption/desorption at electrolyte/electrode interface as electric double layer, while pseudocapacitors relies on reversible redox reactions occurring at the electrode surface to store energy. The majority of current available supercapacitors are EDCLs because of the absence of chemical reactions, simple mechanism, and longer cycle life comparing to pseudocapacitors [7][10].

Carbonaceous materials, such as carbon nanodots (zero-dimensional), carbon nanotubes (one-dimensional), graphene (two-dimensional), and porous carbons (three-dimensional) have been prepared to achieve higher capacitive performance due to their high electrical conductivity, excellent chemical stability, and high surface area [11]–[14]. It is noteworthy that porous materials could be considered as potent material as electrodes in electrical double-layer capacitors (EDLCs) because of promoting electro-

2

sorption of electrolyte ion to form effective electric double layer [15]-[17]. Renewable carbon-based electrodes from biomass resources is in urgent demand to be produced from environmental and energy point of view. BiomasSs-derived materials mostly exhibit developed electrochemical characteristics compared to mentioned various carbon types [18]. Regarding to environmental and energy impacts of biomass derived carbon materials, many natural precursors were used to produce carbon materials, such as banana fibers [19], corn grains [20], fire wood [21], and sugar cane bagasse [22]. Sucrose, as a carbohydrate, could be an attractive carbon source due to its carbonization through dehydration to get carbon. Carbons obtained from sucrose have unique properties such as local availability, free from impurities, and very low price [23].

1.2 Scope and Objectives of Thesis

The aim of this thesis is to synthesize and characterize boron-doped porous carbon material using sucrose as a carbon precursor with good cycling stability and increased electrochemical properties such as power and energy densities. The scopes of this thesis are:

- Synthesis of porous carbon materials via sustainable approach using sucrose as a carbon precursor.
- Doping of carbon materials by using boron to improve their electronic structure.
- Characterization of synthesized boron-doped porous carbonaceous materials.
- Study of electrochemical and capacitance properties of electrode materials.
- Investigating of relationships between input parameters and performance of the supercapacitor based on artificial neural network.

3

The presented results in this thesis reveals effective and simple approaches for preparation of boron doped porous carbon materials for supercapacitor application.

Chapter 2

LITERATURE REVIEW

In this chapter the basic principles, developments, various electrode materials for supercapacitors will be reviewed.

2.1 Types of Supercapacitors

Electrochemical supercapacitors based on their mechanism of energy storage and electrode materials are classified as electrochemical double layer capacitors (EDLC), psudocapacitors and hybrid capacitors [24].

2.1.1 Electrochemical Double Layer Capacitors (EDLCs)

In EDLCs, by applying voltage across the electrodes, the positive and negative charges accumulate based on electrostatic interactions at the interface between electrolyte and surface of electrode. Surface area is one of the most important factors for the electrode materials that improves the storage capacity of EDLCs. Regarding to this point, carbonaceous materials with high porosity are commonly used as electrode materials. Figure 2.1 demonstrate the various compartments of a double layer capacitor.
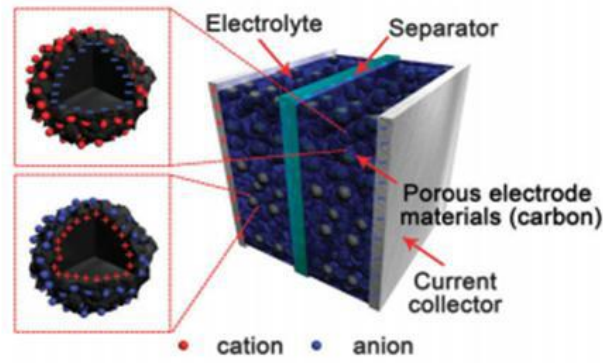
Figure 2.1: different compartment of electrochemical double layer capacitors (EDLCs) [24]

In EDLCs, storing the electrical energy is based on the ion adsorption through electrostatic process in the absence of faradic charge transfer. This characteristic of EDLCs lead to improved power density, quick charge-discharge process, and magnificent cycling stability. In general, following equatsions are expressed the process [25][26]:

On the positive electrode side:

$$E_{S1} + A^- \xrightarrow{\text{Charging}} E^+_{S1}//A^- + e^- \tag{2.1}$$

$$E^+_{S1}//A^- + e^- \xrightarrow{\text{Discharging}} E_{S1} + A^- \tag{2.2}$$

On the negative electrode side:

$$E_{S2} + C^+ \xrightarrow{\text{Charging}} E^+_{S2}//C^+ \tag{2.3}$$

$$E^+_{S2}//C^+ \xrightarrow{\text{Discharging}} E_{S2} + C^+ + e^- \tag{2.4}$$

The general equations of charging and discharging process are revealed as follow:

$$E_{S1} + E_{S2} + A^- + C^+ \xrightarrow{\text{Charging}} E^+_{S1}//A^- + E^+_{S2}//C^+ \tag{2.5}$$

$$E^+_{S1}//A^- + E^+_{S2}//C^+ \xrightarrow{\text{Discharging}} E_{S1} + A^- + E_{S2} + C^+ \tag{2.6}$$
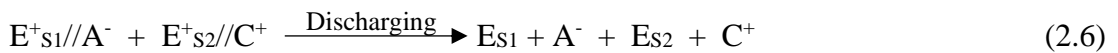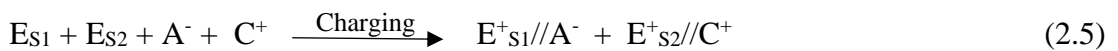
Where, electrode number 1 and 2 represent by E_{S1} and E_{S2}, respectively, // shows interface between the electrode surface and electrolyte ions, A^- and C^+ are charged particles (anion and cation).

Generally, during charging of system the electrons migrate from negative electrode to the positive one. Inside the electrolyte, anions and cations migrate from the negative to positive electrodes respectively and form the double layer as represented by electrode//electrolyte in the 1.5 equation. On the contrary, during discharging the reverse process occurs. So, in this type of capacitors, there is no charge transferring and also any ion exchanges across the electrode and electrolyte (electrode//electrolyte) interface. It reveals that the concentration of electrolyte would be constant during the whole charge and discharge process [25][26].

2.1.2 Pseudocapacitors

In this type of capacitors, the energy storage is based on faradic process which is reversible redox reaction happening at or close to the electrode surface.

The redox reaction is so quick and this kind of electrochemical devices mostly carbonaceous materials with remarkably high capacitance. Figure 2.2 demonstrate the schematic of pseudocapacitors.
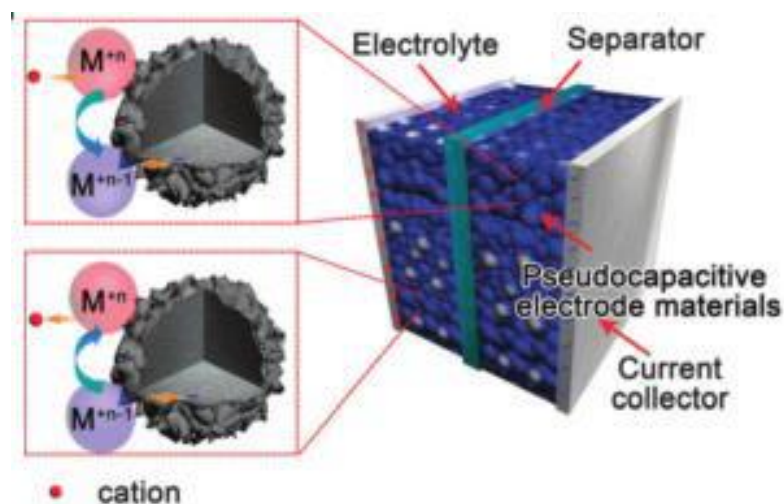
Figure 2.2: Schematic of pseudocapacitors [24]

Many different mechanisms happening in pseudocapacitors have been recognized [27]. These mechanisms are because of various physical processes and different materials types (Figure 2.3).
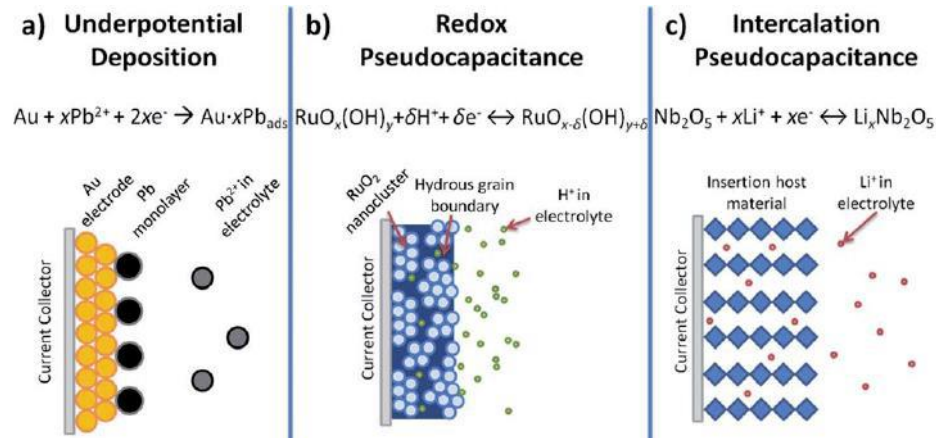
Figure 2.3: Three various models of redox mechanism in pseudocapacitors [27]

The mechanisms involve:

a) Under potential Deposition: in this case metal ions form a monolayer on the surface of other metal upper than their redox potential. For instance, deposition of Pb on the surface of gold.

b) Redox Pseudocapacitance: electrochemically adsorption of ions occurs close or on the electrode's surface by quick faradic charge transfer. For example, hydrogen storage by hydrated RuO_2.

c) Intercalation Pseudocapacitance: this mechanism is based on the penetration of ions to the channels or layers of electrode consist of redox active material and at the same time occurring faradic charge transfer without phase separation.

2.1.3 Hybrid Capacitors

As the name implies, the mechanism of energy storage in hybrid supercapacitors are based on electrostatic and faradic process. Figure 2.4 shows the schematic of a hybrid capacitor (lithium ion).
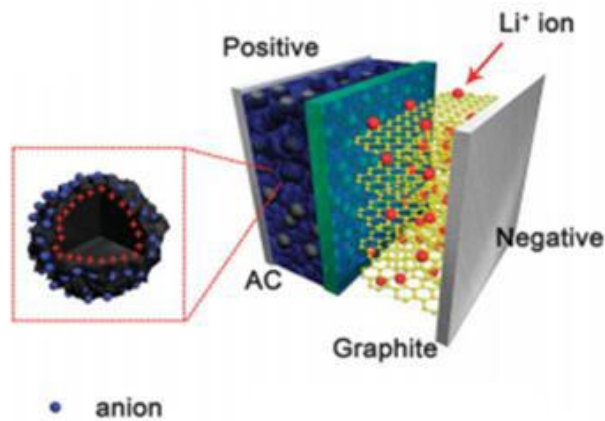
Figure 2.4: Schematic of a hybrid capacitor (lithium ion capacitor) [24]

In this kind of capacitors, different anode and cathode electrode materials were used. Asymmetric configuration of electrode materials leads to wider potential window. It is due to using of two complementary different electrode materials by various potential window and causing increase in operating voltage. Hybrid capacitors are designed asymmetric which consist of a EDLC electrode (commonly activated carbon) and the other electrode material is a kind of battery type electrode (PbO_2, $Ni(OH)_2$, TiO_2, metallic lithium, etc.) [24] such as carbon//$RuO2$ [28], carbon//titania, and carbon//$Ni(OH)_2$ [29]. Recently, new kind of hybrid capacitors are designed like lithium capacitors (LIC) [30], and carbon//lead oxide capacitor [31]. Furthermore, combination of electrodes such as a lithium metal as a rechargeable battery type and a pseudocapacitive electrode as a positive electrode such as MnO_2 lead to asymmetric hybrid capacitors [32].

2.2 Fundamentals of Working and Evaluation Methods (Experimentally) of Supercapacitors

2.2.1 Mechanisms of Energy Storage

Supercapacitors based on their mechanisms of energy storage are grouped in two categories: electrical double layer capacitors (EDLCs) and pseudocapacitors. Briefly,

in EDLCs the mechanism of capacitance is accumulation of electrostatic charge at electrolyte/electrode interface. While, the mechanism of capacitance for pseudocapacitors relies on the redox process because of electro active materials. Sometimes the combination of these two mechanisms are used which is known as hybrid capacitors. In the following sections, energy storage mechanisms of supercapacitors are going to defined in detail.
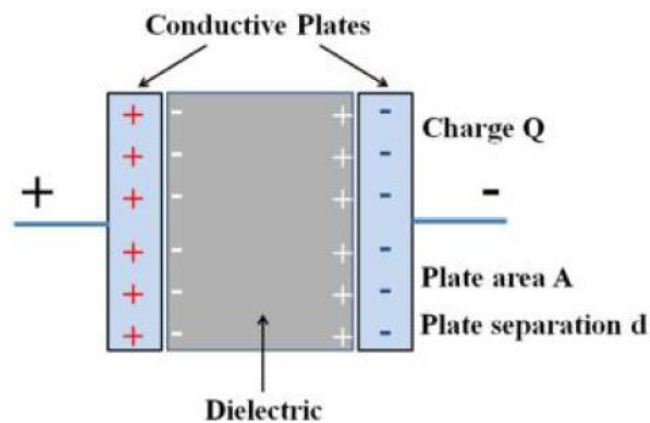
Figure 2.5: Schematic of a parallel-plate capacitor

Conventional capacitors widely known as a device composed of two electrically conductive plates and separated by dielectric, and electric charges are stored and accumulated between and on the surface conductive plates. Figure 2.5 shows the schematic of a conventional capacitor. Accordingly, energy storage of conventional capacitors is too low due to the low surface area of plates and also geometric constrained space between the charged plates. On the contrary, EDL capacitors can store more energy due to the large surface area of electrode materials and separation distance in atomic scale. As shown in Figure 2.6, Stern (1920s) modified and developed the EDL model on the basis of Gouy, Helmhotz, and Chapman studies [33]. In stern model two cleared regions were recognized, Stern layer or inner compact layer and diffuse layer or the outer region. In Stern layer (compact layer), ions, mostly

hydrated, stored and adsorbed strongly on the electrodes. The stern layer composed of particularly absorbed ions called inner Helmholtz plane (IHP) and unparticular adsorbed ions in the outer Helmholta plane (OHP). Diffuse layer is a region close to the electrode, where distribution of ions in electrolyte happened through kinetic motion inside the electrolyte.

The total capacitance of double layer C_{dl} includes capacitance of stern mode compact double layer (C_H) and capacitance of diffuse region (C_{diff}):

$$\frac{1}{C_{dl}} = \frac{1}{C_H} + \frac{1}{C_{diff}}$$

(2.7)

The EDL performance at electrode surface relies on several factors such as electrical field, fundamental properties of electrolyte and electrode, and affinity (chemical) between the electrode surface and adsorbed ions.
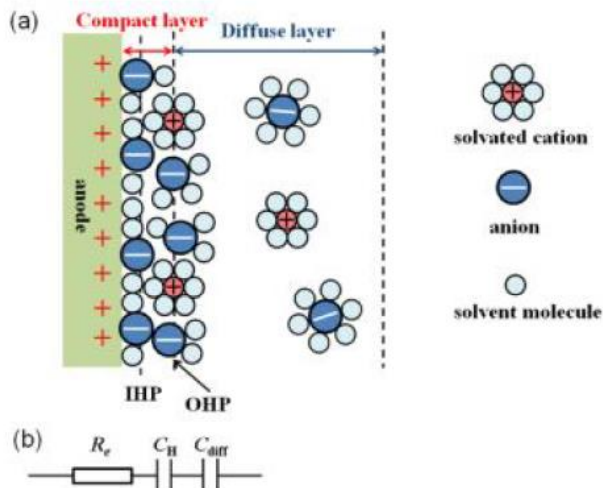
Figure 2.6: Schematic of Stern model of the double layer region. IHP (inner Helmholtz plane), OHP (outer Helmholtz plane)

Capacitance calculation of EDLCs is based on the parallel-plate capacitor, expressed by the following equation:

$$C = \frac{Q}{V} = \frac{\varepsilon_0 \varepsilon_r}{d} A$$

(2.8)

Where Q is the total amount of charge on the plates, V is the voltage imposed across the capacitor, A ($m^2 g^{-1}$) is the specific surface area of accessible interface of electrode-electrolyte to the ions, d (m) is the effective thickness of the EDL (Debye length), ε_0 is the permittivity in vacuum and ε_r (a dimensionless constant) is the electrolyte dielectric constant. Energy storage mechanism of carbonaceous materials mainly obey the EDLC rule.
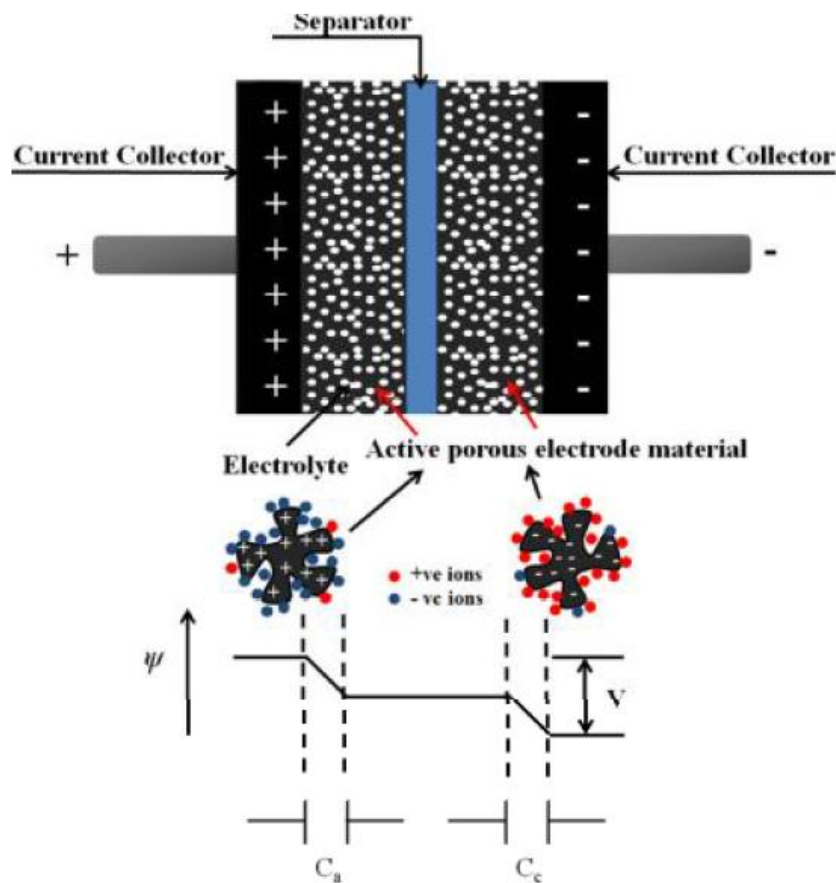
Figure 2.7: represent Schematic of an EDLC system on the basis of a porous electrode material and illustrate the dropping of potential at interface of electrode-electrolyte

During the process of charging, electrons migrate from negative electrode through an external circuit to the positive electrode. Inside the electrolyte, cations travel to the negative electrode while the anions travel to the positively charged electrode. On the other hand, reverse process occurs in discharging process. It can be concluded that

mechanism in EDLCs are physically adsorption of ions without any charge exchange or transfer between the electrolyte and electrode.

In pseudocapacitance comparing to the EDL capacitance, thermodynamic terms arise to describe the capacitance such as stored charge Δq and potential change ΔV as shown in following equation:

$C = d(\Delta q)/(d\ \Delta V)$ (2.9)

By applying a potential to pseudocapacitor system, on the electrode quick and faradic reaction (reversible) occur and charges passing across the electrolyte/electrode interface. Faradic processes in pseudocapacitors in contrast with batteries involves thermodynamic of potential change while charge accumulation and lead to having better reversibility and higher power [34].

Faradic processes happening at pseudocapacitive electrodes are: (1) adsorption of metal ion or proton from electrolyte reversibly; (2) redox reactions of electrolyte ions; and (3) reversible doping-undoping process at conductive polymer-based electrode [33]. In the meantime, components with EDL capacitance process (proportional to interfacial area) mostly convoy with redox reactions.

Functional groups on the surface of carbon materials are the mostly common active species, electrically conductive materials, and transition metals (in oxides form) like ruthenium oxide, vanadium nitride, and manganese oxide. Principally, pseudocapacitors generate more energy density compared to EDLCs, particularly in the systems containing metal oxides with various oxidation states. Conway et al. reported capacitance of pseudo type capacitors are 10-100 times more than the EDL capacitors [35]. On the other hand, pseudocapacitors mostly suffer from instability

during cycling and low amount of power density because electrodes during charge/discharge process change physically and also slow redox reactions (faradaic process).

2.2.2 Evaluation Methods for Supercapacitors

The configuration of a supercapacitor is so similar to the batteries. Figure 2.8 shows a supercapacitor (single cell) composed of separated electrodes (by separator) in touch with the electrolyte. The whole cell could be considered as two separated capacitors in a series. Figure 2.8 shows a circuit presentation of capacitor (single cell) equivalent resistor capacitor (RC). C_c, C_a, and R_s are representing of the cathode, anode, and equivalent series resistance (ESR) respectively. R_F representing self-discharge resistance of an electrode. The calculation of the total capacitance of whole cell is shown as following equation:

$$\frac{1}{C_T} = \frac{1}{C_a} + \frac{1}{C_C}$$
(2.10)
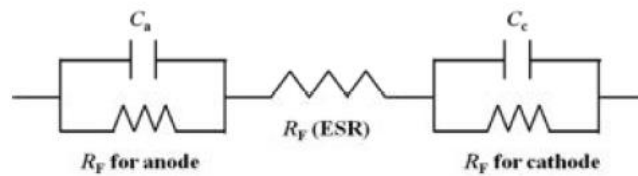
Figure 2.8: Circuit presentation of capacitor (single cell) equivalent resistor capacitor (RC)

In symmetric supercapacitors, If the same electrodes are selected, Ca and Cc would be equal and total capacitance (C_T) equal to half capacitance of for each electrode. On the other hand, in asymmetric capacitors, using different materials for cathode and anode, electrode capacitances are not equal and C_T determined by the electrode with smaller capacitance [25]. Generally, charge storage and capacitance fundamentally rely on electrode materials.

The maximum energy storage (E) and power density (P) for a common supercapacitor (single cell) are expressed as following equations:

$$E = \frac{1}{2} C_T V^2 \qquad (2.11)$$

$$P = \frac{V^2}{4R_s} \qquad (2.12)$$

where V and C_T represent the voltage (in volts) and total capacitance (in farads) of the cell, respectively and R_s represents the ESR (in ohms).

It is clear from the equations that CT, V, and RS are the three important factors effect on the performance of a supercapacitor. The voltage of a cell depends on the electrode material and also affected by thermodynamically stability of electrolyte. ESR originated from different kinds of resistance due to the intrinsic electronic characteristics of electrolyte and electrode material, resistance of ions due to the mass transfer in the matrix, and contact resistance of electrode and current collector [5]. In order to enhance the capacitance of overall cell, capacitance of the electrodes should be increased. Accordingly, high performance supercapacitors should possess great capacitance value, high operating voltage, and the least ESR. Therefore, it is clear that investigating and developing of electrolyte and electrode materials are crucial to optimize the performance of supercapacitors.

2.3 Experimental Evaluation: Principles and Methods

2.3.1 Cyclic Voltammetry (CV)

In general, rectangular CV curve demonstrate the capacitance relies on the EDL while no faradic reaction happened. Calculation of specific capacitance is based on the scan rate (v) and current (I), at the center of potential range. Following equation represent the calculation of specific capacitance:

$$CT = \frac{1}{mv} \qquad (2.13)$$

Where m is the active material mass. On the other hand, pseudocapacitive mostly deviate from the rectangular form which may contain redox peaks. Therefore, calculation of average capacitance is based on utilizing voltammetric charge through integration of the CV curve, based on the following equation:

$$C_T(Fg^{-1}) = \frac{Q}{2mV} = \frac{1}{2mVv} \int_{v-}^{v+} I(V)dV \qquad (2.14)$$

Where Q is the charge (in C, area under the curve of CV), active material mass of two electrodedes is shown by m (in g), v is scan rate (in V s^{-1}), and V is potential window of negative and positive electrodes in V s^{-1} (V= V^{+}-V^{-}) [36].

2.3.2 Galvanostatic Charge-Discharge (GCD)

In GCD method, generally the potential is proportional linearly with the time of charge and discharge time in constant current process (dV/dt = constant). Following equation express the total capacitance:

$$C_T = \frac{I}{mdV/dt} \qquad (2.15)$$

Where, I (A) represent discharge current, m (g) is active materials mass (both electrodes), and dV/dt represent the discharge curve slope. Regard to nonlinearity relation between time and potential in pseudocapacitive process, two data set should be used from discharge curve to calculate the specific capacitance (dV/dt = (V$_{max}$-1/2V$_{max}$)/(t$_2$-t$_1$)) [6]. Where, Vmax is the maximum potential, t$_1$ and t$_2$ (s) are discharging times at V$_{max}$. In some literature, following equations are used to express the maximum power and energy density [37].

$$E_{max} = \frac{0.5\, C_T\, V^2}{3.6} \qquad (2.16)$$

$$P_{max} = \frac{E_{max} \times 3600}{t} \qquad (2.17)$$

2.3.3　Electrochemical Impedance Spectroscopy (EIS)

EIS is one of the most important tools to examine the behavior of supercapacitors and ESR. EIS is measured in an open-circuit potential (OCP) process by implementing a perturbated small-amplitude AC over a frequency range. The resistance is expressed by the following equation:

$$Z = Z' + jZ'' \tag{2.18}$$

In this quation, Z'' and Z' are the imaginary and real part of impedance, respectively. Total specific capacitance is also can be calculated from collected EIS data and Z'' according to the following equation:

$$C_T = -\frac{1}{2\pi f Z'' m} \tag{2.19}$$

Where f and m are frequency (in Hz) and mass of electrode materials, respectively.

EIS commonly expressed by the Nyquist plot (Z'' against the Z'). The obtained intercept from Nyquist plot the ESR can be found which suggesting the conductivity of electrolyte and active material of electrode. At high frequency a semicircle represents a supercapacitor with pseudo-manner. In addition, inside the electrode material there is contact resistance and also the interaction between electrode and electrolyte can cause resistance. At lower frequency range a line with 45º slope represent the ion diffusion relies on the redox reactions on the electrodes or diffusion of ion diffusion of electrolyte into the electrode. A vertical like line at low frequency mostly represent an ideal capacitor characteristic. Figure 2.9 shows the Nyquist plot and corresponding circuit to interpret the mentioned parameters quantitively. In the circuit, C_L represent the limit capacitance, Warburg impedance shown by W, R_b represent the uncompensated resistance including electrolyte resistance, R_e represent charge-transfer resistance, and C_e is capacitance by double layer behavior.
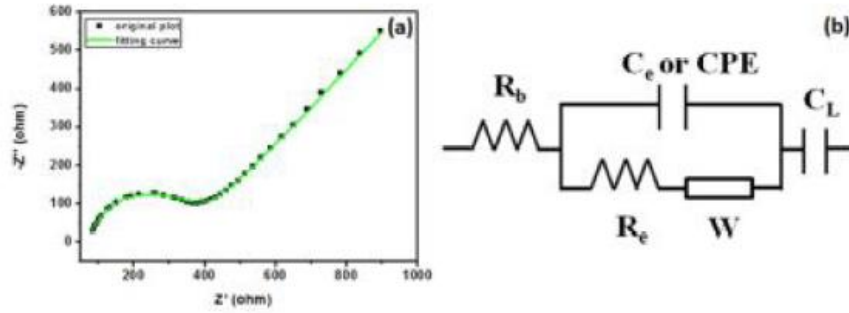
Figure 2.9: (a) Nyquist plot and (b) Its circuit for impedance analysis

Notably, interpreting and analyzing of EIS for materials with pseudocapacitive behavior and complex kinetics would be carried out case by case. In this kind of materials even the semicircle is not perfect [38]. For two electrode and packaged cells, generally by the help of GCD results the ESR is determined by using IR drop. The value of ESR is determined by dividing the voltage change (IR drop) and changes in applied current. Generally, to stabilizing the voltage before starting discharge, the starting current is set approximately zero. In some cases that the current is changed instantly from totally charged to completely discharged, Rs is calculated by dividing the outcome voltage drop to twice the applied current according to following equation [39]:

$$R_S = \frac{V_{drop}}{2I} \tag{2.20}$$

2.4 An Overview of Carbonaceous Materials for Supercapacitor Electrodes

Carbonaceous materials among different kinds of materials containing carbon and organic matters, stand out as one of the best electrode candidates for supercapacitors due to their promising characteristic features such as, electrical conductivity, low price, chemical stability, easy functionalization. Nowadays, the most of commercial supercapacitors composed of porous carbon materials as electrodes [40].

Carbonaceous materials are representing various kind of materials such as carbon dots (zero dimensional) [41], carbon nanotubes (one dimensional) [42], graphene (two dimensional) [43], carbon foams (three dimensional) [44], polymer fibers [45], and biomass derived carbon materials [46].

The ultimate aim in supercapacitor research is to reach very high capacitance (charge storage) at ultra-high number of scan rates. Carbonaceous materials are the best candidate among other materials to achieve the mentioned aim due to their high electrically conductivity. Very low electrical resistance facilitates the quick electron transport and transfer, which is crucial for the supercapacitors with high rate performance. For decades the gravimetric capacitance of studied carbon materials had remained at a moderate level (100-200 $F.g^{-1}$) [47]. It is found that the main reason for the limited energy density and capacitance is due to the low specific surface area or small ion accessible area of designated carbons. Factors that resulted to limited ion-accessible area are insufficient intrinsic surface area and accessibility of ions are restricted to some extent of area. For instance, specific surface area of woven carbon cloth by carbon fibers (micron size) is around 5.0 m^2g^{-1} [48]. Although, surface area of activated carbon is around 1000 m^2g^{-1} but most of micro pores are rarely accessible for ions and its gravimetric capacitance is around 100 F g^{-1} [49]. In addition, the specific capacitance could be decreased through enhancing the current density and scan rate. Thus, it is crucial to extend the accessibility of ions to the surface area of carbonaceous materials by maintaining pathways of charge diffusion to reach high capacitance values ultraquick charging rates.

To overcome aforementioned challenge hierarchical porous carbon materials introduced. They have interconnected multi-scale pores and gathered into hierarchical

pattern. The multi-scaled pores facilitate diffusion of ions and infiltration of electrolyte, so improves the accessibility of ions to the entire electrode and even their capacitance exceeds to around 300 F g^{-1}.

2.5 Hierarchical Porous Materials

Hierarchical porous materials should contain multi scale pores and at least two types of pores. Pores are classified according to the pore width by IUPAC in 1985. Pore width explained as pore diameter and inter layer distance. Based on IUPAC pores are categorized into three classes [50]:

- Macropores, more than 50 nm pore width;

- Mesopores, between 2-50 nm pore width;

- Micropores, less than 2 nm pore width.

By developing nanomaterials, IUPAC introduce new pore types in 2015 [51]:

- Nanopores, smaller than 100 nm pore width;

- Supermicropores, between 0.7- 2 nm (large micropores);

- Ultramicropores, smaller than 0.7 nm pore width (small micropores).

According to the new classification, nanopores materials containing mesopores, micropores, and macropores with limit of 100 nm for pore width. Figure 2.10a shows the schematic of pores classifications.

Porous system with only different pore sizes are not qualified as hierarchal porous material. The term "hierarchy" refers to a material that clearly present interplay among all various pores and forming hierarchical network. Presence of various interconnected types of pores is crucial for supercapacitors that the basis of their operation is based

on the ion diffusion. Figure 2.10b shows the ion diffusion pathway in hierarchical porous system. Firstly, ions diffuse to the largest pores and gradually enter to the smaller ones. It continues till all ions reach to the smallest ones.
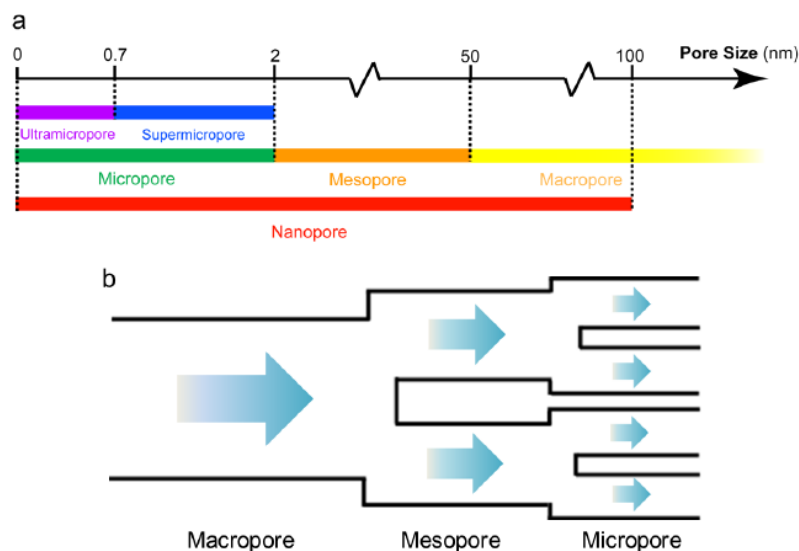
Figure 2.10: (a) Classification (IUPAC) of pores according to the pore width (b) Schematic pattern of ion diffusion into hierarchical porous systems

2.6 Biomass Derived Carbon Materials

Natural biomass resources mostly represent hierarchical structure, which make them one of the best candidates to prepare carbon materials with desirable characteristics for batteries and supercapacitors. At the same time, biomass resources are highly accessible and recyclable materials which can be used as precursor to prepare biofuels like bioethanol and biodiesel and also converted to green carbon materials by various methods such as chemical activation, physical activation, and hydrothermal carbonization (HTC) [52]–[54]. Actually, most of derived carbon materials from biomass resources possess unique properties like high porosity and excellent conductivity and make them as highly potent materials in various application such as catalysis, environmental purification, and energy storage [55], [56]. Nowadays, with

respect to energy storage challenge many studies have been conducted to synthesize nanostructured active carbon materials from natural and renewable resources.

2.6.1 Biomass Resources

Generally, all living and biologically materials are a kind of biomass materials. Figure 2.11a shows various biomass resources such as agriculture and energy corps, wood, animals, and municipal wastes, algae and aquatic plants [57]. In general, biomass is able to transform solar energy to chemical energy and store it by photosynthesis mechanism. Thus, biomass energy is an important kind of renewable energy resources such as wind, solar, and geothermal. Noteworthy, by using these kinds of energies no CO_2 will add to the environment [58].

To date, by increasing the energy usage demand such as cooling, heating, vehicle fueling, and electricity generating, energy produced by biomasses are crucial.
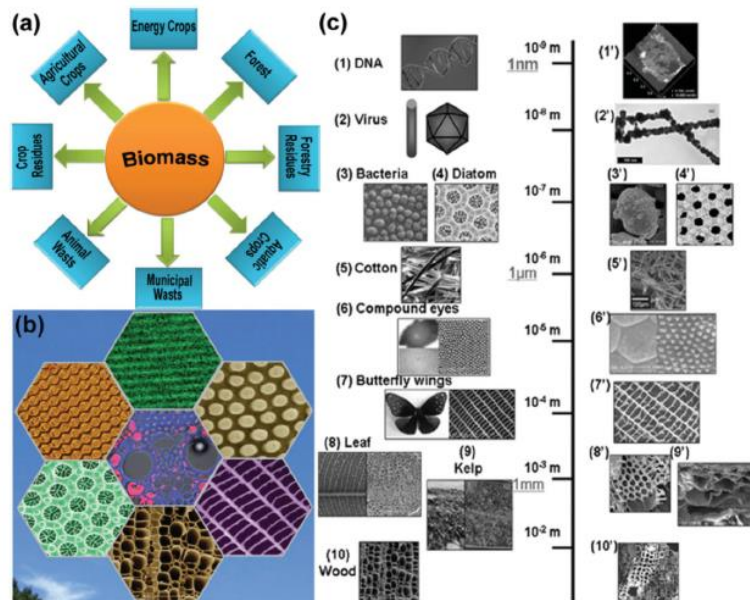
Figure 2.11: (a) Naturally biomass resources. (b) Different naturally microstructure biomaterials. (c) Biological materials based on their length scale [58]

Biomass materials are not be able to used directly by burning or converting them to gas or liquid fuel like biodiesel [59]. On the other hand, biomasses are used as precursor to synthesize new sustainable and green materials in terms of energy [60]. Regular products from biomass materials are activated carbons (ACs) and biochar. Biochar mostly prepared by pyrolysis or burning in low presence of oxygen which leads to highly porous material with acceptable surface area. The benefit of this kind of porous materials is to absorb nutritive anions and cations to grow the microorganisms of soil and enhancing soil fertility in agriculture application [61]. Other by-product of pyrolysis of biomass materials is activated carbons with high porosity and surface area which is applicable in various study fields such as water purification, gas separation, catalysts, fuel cells, and electrode material for supercapacitors [62].

In addition, biomass materials mostly present interesting structures like nanoarchitectures and hierarchical organization. Figure 3(b,c) shows carbonaceous materials with controllable morphology for environment and energy application [63].

2.6.2 Conversion Method

Till now, different methods have been applied to convert biomasses materials to energy. Generally, all the conversion methods can be classified in two processes, thermochemical (i.e. pyrolysis, gasification, and combustion) and biochemical (i.e. anerobic digestion and fermentation) [64]. One of the most important form to recovery of energy and also potent to produce various kind of materials for instance gas, char, and oil [65]. In the process of pyrolysis, first the adsorbed water and also volatile compounds of prepared materials are evaporated and solid char with different properties comparing to the original biomass are remained. Thus, produced char form

pyrolysis process can be used as precursor to prepare different carbon materials such as porous carbon, activated carbon, fullerenes, carbon nano tubes, and graphene [66]–[69]. In addition, functional groups present on the surface of prepared carbon materials can be modified by various agents and activation methods [52][70]. The obtained carbon materials from biomass are potent to take benefit in various applications such as waste water treatment, air pollution control, catalysts, and energy storage and conversion. In general, three major activation methodologies to prepare carbonaceous materials from biomass materials include chemical activation, physical activation and hydrothermal carbonization (HTC). Briefly, the conversion methods are summarized.

2.6.2.1 Physical Activation

Physical activation is the most common process to produce active carbon. It consists of two steps, first pyrolysis of raw materials (< 1000 K), second step followed by gasification at higher temperature (higher than 1000 K) by oxidizing gases (CO_2, air, and steam) [71]. Raw materials at the first step of carbonization are heated up at moderate temperature and under inert atmosphere. Figure 2.12(a) shows the weight loss evaluation of three kinds of cellulosic precursors through carbonization process [72]. All the three materials during weight loss exhibit similar trend by enhancing the temperature. Three main stages exist:

(1) Quick weight loss corresponds to moisture and water ($\sim$300K - $\sim$470K)

(2) Mild weight loss corresponds to early pyrolysis ($\sim$470K - $\sim$770K)

(3) Mild weight loss related to stabilization of char structure ($\sim$770K - $\sim$1120K)

In carbonization process, pores of the produced char are filled by disordered carbon due to the decomposition and leads low surface area and close (inaccessible) pores which could be a disadvantage of these type of carbon materials. Hence, further

activation is needed to achieve improved and reachable porosities through gasification of obtained char at higher temperature. In physical activation CO_2 or H_2O are used as activation gas because these gases are easy to handle and clean [73]. Various raw materials were used to produce activated carbon by physical activation method such as rice straw, rice husk, corn hulls, corn cob, pecan shells, peanut hulls, almond shells, and coconut shells [62][68][74][75].
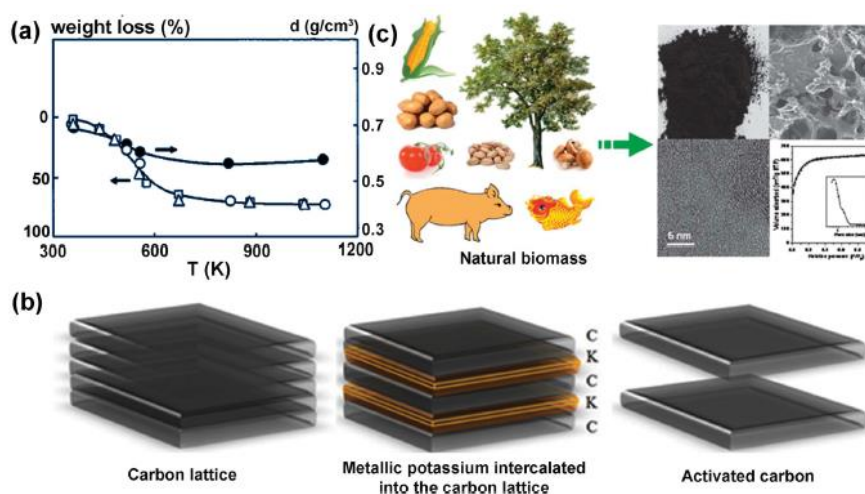
Figure 2.12: (a) Almond shells, peach stones, and olive stones weight loss during carbonization. (b) Mechanism of activation above 1000 K through potassium penetration into the carbon lattice [75]

2.6.2.2 Chemical Activation

Chemical activation is a single step which activation and carbonization perform at ~700-~1200K and precursor mixed with some activating agents such as KOH, $ZnCl_2$, K_2CO_3, and H_3PO_4 [76]–[79]. Carbon materials obtained from chemical activation represent large pore volume and remarkable surface area (>2000 m^2 g^{-1}). Chemical activation in comparison with physical activation has shown several advantages such as less activation time, higher surface area, lower processing temperature, more carbon yield and porosity.

25

Notably, KOH is the most common activating reagents due to its higher yield and low activation temperature. Activated carbons obtained from this method show great pore size distribution and excellent surface area (more than 3000 $m^2 g^{-1}$) [53].

In this methodology the mechanism not completely understandable due to different variables and precursors. So, we present here activation mechanism of activated carbon through KOH. Typically, the reaction of raw materials and KOH is a kind of solid with solid reaction, followed by some solid with liquid reactions and finally potassium would be converted to metallic potassium through reduction reaction.

As an example, the following equations represent KOH activation of petroleum coke at below 1000 K [80]:

$$2KOH \longrightarrow K_2O + H_2O \quad\quad\quad (2.21)$$

$$C + H_2O \longrightarrow CO + H_2 \quad\quad\quad (2.22)$$

$$CO + H_2O \longrightarrow CO_2 + H_2 \qu\quad\quad (2.23)$$

$$CO_2 + K_2O \longrightarrow K_2CO_3 \qu\quad\quad (2.24)$$

$$6KOH + 2C \longrightarrow 2K + 3H_2 + 2K_2CO_3 \quad\quad\quad (2.25)$$
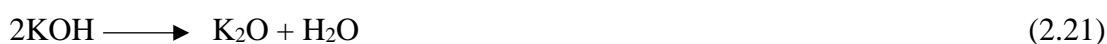
In the first stage (Equation 2.20), KOH is converted to the K_2O through dehydration reaction at less than 700 K while the carbon precursors are reacted by H_2O and produced CO_2 and H_2 (Equation 2.21 and 2.22). Next step (Equation 2.23) by reaction of $CO2$ and K_2O, K_2CO_3 is formed. By increasing the temperature over 900 K, metallic potassium formation is started (Equation 2.24).

$$K_2CO_3 \longrightarrow K_2O + CO_2 \quad\quad\quad (2.26)$$

$$CO_2 + C \longrightarrow 2CO \quad\quad\quad (2.27)$$

$$K_2CO_3 + 2C \longrightarrow 2K + 3CO \quad\quad\quad (2.28)$$

$$C + K_2O \longrightarrow 2K + CO \quad\quad\quad (2.29)$$

26

In equation 2.24, by increasing temperature to more than 1000 K, decomposition of preformed K_2CO_3 is started and leads to form carbon dioxide and potassium oxide and totally removed at around 1100 K. In equation 2.25, carbon dioxide is reacted with carbon and reduced to carbon monoxide. Finally, in equation 2.26 and 2.27, K_2CO_3 and potassium oxide are reduced by carbon and potassium in metallic form is formed.

Generally, activation by potassium hydroxide consist of three main stages:

1- Reaction of carbon with potassium containing compounds (Equations 5, 8, and 9), which form carbon material containing porosity network (chemical activation).

2- By mixing of H_2O and CO_2, hot steam is formed at high temperature (Equations 1, 3, and 6). It is called physical activation that assist development of carbon porosity (Equations 2 and 7).

3- The metallic potassium enters the carbon framework (Equations 5, 8, and 9) and carbon lattices are expanded as shown in figure 4(b).

Different raw materials have been used to produce activated carbons via chemical activation such as pitches, peat, coal, cokes and also from renewable biomass materials like rice husk, saw dust, nut shells corncob, and rice straw [62][81][82]. Especially, Figure 4 (C) shows various activated carbons by KOH from natural biomass resources, such as scale of fish, wheat straw, flour, banana peel, fungi, and pig bone [83]–[91].

2.6.2.3 Hydrothermal Carbonization (HTC)

Naturally coal or peat obtained from plants or biological materials during long time (million years) via natural chemical coaling reactions. Some efforts have made to imitate coaling process and forming carbon materials from natural biomass resources by faster processes. Particularly, HTC is a method to transform cellulose to carbon

materials (coal-like). It was reported for first time in 1913 by Bergius and then developed further in 1932 by Schmidth and Berl [92]. Nowadays, HTC is one of the promising methods to obtain carbonaceous materials from biomass sources under normal conditions at moderate temperature (below 500 K), self-produced pressure and water solution [52][93]. HTC comparing to other conventional activation processes (chemical and physical) is one of the crucial alternative methods to obtain carbonaceous materials due to its unique characteristics such as mild synthesis process, cheap, and environmentally friendly process.

To understand the fundamental of HTC process various carbohydrates (sucrose, starch, glucose, furfural, hydroxymethylfurfural, and xylose) were used as precursor to obtain carbon materials at 180 °C (hydrothermal conditions) [94]. The structural composition and morphology of obtained carbon materials were investigated by elemental analysis, solid state ^{13}C-NMR, and scanning electron microscopy (SEM). To analyze the unreacted species and side products of in liquid solution, mass spectroscopy and gas chromatography were also used. The results demonstrate that all types of sugars (Hexose) were converted to carbonaceous form with close chemical composition (Figure 2.13). Additional experiments reveal that all kinds of precursors (natural biomass or pure sugar) converted to same outcome in terms of structure and morphology. According to mentioned experiments, HTC reactions consist of three steps:

1- Transforming of carbohydrates to hydroxymethyl furfural via dehydration reaction.

2- Formation of polyfurans through polymerization.

3- Carbonization of polufurans via intermolecular dehydration.

At the end, the final solution start to change the color from brown to dark and spherically shape carbons were obtained. The obtained carbons can be used for further functionalization by polar functional groups and making carbons more hydrophilic and easier to disperse in water.
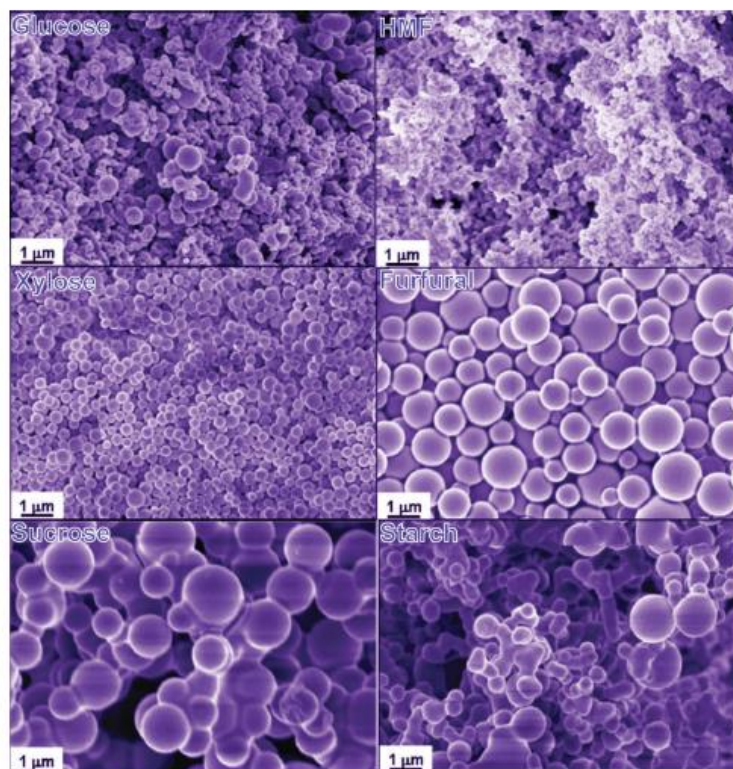
Figure 2.13: SEM of different obtained carbon through hydrothermal carbonization [94]

HTC process provides porous carbon materials from biomass precursors and considered as cheap process [55][93]. On the other hand, comparing the carbonaceous materials obtained from HTC with other activated carbons (chemical and physical) show less porosity and specific area, which is not grateful to use as adsorption, catalysis, and energy storage applications. So, controlling porosity at nano-scale is necessary by addition of different templates such as SBA-15 or addition of activating

agents such as KOH during the process helps to improve the surface area and porosity [95][96].

2.7 Carbonaceous Materials Derived from Biomass Resources for Supercapacitors

Supercapacitors, also well known as electrochemical capacitors or ultra-capacitors, have shown excellent properties such as remarkable charge-discharge, great power density, low cost maintenance, and superior lifespan and considered as good candidate for storing energy device for electric vehicles and electronic devices [97]. According to the mechanism of storage supercapacitors classified in two main groups: (I) EDLCs, based on accumulation of charges on the surface of electrodes and (II) Pseudocapacitors, based on reversible and fast redox reaction at specific potential [98]. Development of supercapacitors performance relies mainly on the electrode materials. Carbonaceous materials, transition metal oxides, and conducting polymers, have been considered as the most potent as electrode materials [25][99]–[101]. It should be emphasized that various kinds of carbonaceous materials ranging from conventional ACs to developed nanostructure carbons (CNTs and graphene) have been used as potent electrode materials due to their unique physicochemical characteristics such as great chemical stability, excellent electron conductivity, ultrahigh surface area, and controllable porosity [17]. From environmental and energy point of view, developing of straightforward an environmentally friendly techniques to prepare carbonaceous electrode materials is necessary. Many studies have been conducted to prepare renewable carbonaceous materials from biomass resources. The prepared electrodes from biomass materials mostly represent acceptable electrochemical properties comparing to the conventional ACs, carbon fibers, carbon nanotubes, and graphene.

Nowadays, it is a great attention to prepare carbonaceous materials from different kinds of biomass sources and their application in supercapacitors as electrodes due to easy access and cheap resources [102]–[104].

As natural biomass, sucrose has been widely considered as a low-cost attractive carbon precursor [23][105]–[108]. For instance, Navaladian et al. [108] synthesized sucrose-based nitrogen doped activated carbon at a high temperature, the electrode material exhibited a specific surface area of 518 m2 g−1 and a specific capacitance of 277 F g^{-1} at 0.5 A g^{-1}. Likewise, Zhou et al. [109][12] prepared a high surface-area (1751 m2 g−1) nitrogen-doped sucrose-based porous carbon as supercapacitor electrode material. In 6 M KOH, they reported a specific capacitance of 335 F g^{-1} at 1 A g^{-1} and suggested that the large surface area of the electrode, its appropriate porosity and the high nitrogen content generated as pseudocapacitance.

2.7.1 Physical Activation of Carbon Materials Derived from Biomass Resources

One of the most common methods to prepare ACs from biomass resources is thermal or physical activation. Physical activation process consists of two main steps: (I) low temperature carbonization (∼700 K - ∼1150 K) and (II) high temperature activation (∼900 K - ∼1200 K). Additionally, process of physical activation is mostly considered as energy wasting, time consuming and environmentally harmful.

Different kinds of biomass resources were used as precursor to obtain ACs for supercapacitors application such as rubber wood, fire wood, coffee endocarp, and pistachio shell [103][110]. For instance, Nabais et al. prepared ACs from coffee endocarp through physical activation and using CO_2 as activating agent [110]. The prepared ACs show high surface area around 1051 m^2 g^{-1}, large pore volume about 0.49 cm^3 g^{-1}, and reasonable capacitance of ∼175 F g^{-1}. Tear et al. reported rubber

31

wood as biomass precoursor to obtain activated carbon with relatively high surface area of 913 m^2 g^{-1} and 138 F g^{-1} as specific capacitance [111].

2.7.2 Chemical Activation of Carbon Materials Derived from Biomass Resources

Chemical activation involved impregnating of starting material in a single step process by using potassium hydroxide and zinc chloride (activating agent), following moderate heat treatment ($\sim$700 K - $\sim$900 K). obtained ACs show relatively high surface area and micropore porosities. Different biomass resources have been used to obtain ACs for supercapacitor application such as waste paper [112], flour [84], fallen leaves [113], pig bone [83], celtuce leaves [114], sunflower seed shell [115], silk [116], sewage slug [117], fish scale [118], cherry stone [119], water bamboo [120], yeast cells [121], pine-cone [122], waste tea leaves [123], ginkgo shells [124], and human hair [125]. For instance, natural flour was used to obtain AC with honeycomb morphology through KOH activation, which showed high BET surface area of 1312 m^2 g^{-1}, relatively high capacitance around 472 F g^{-1} as shown in Figure 2.14 [84]. Wang et al. used leaves of celtuce as precursor and resulted in very high surface area (3403 m^2 g^{-1}) and pore volume (1.88 cm^3 g^{-1}) ACs. The prepared ACS were used as supercapacitor and CO_2 capture application (Figure 2.14 c). Electrode materials from ACs were used in two and three electrodes systems and represent great capacitance of 270 and 420 F g^{-1}, respectively [123]. Figure 2.14d shows conversion of natural silk to ACs through combination of graphitization and activation, which exhibit ultrahigh surface area (2490 m^2 g^{-1}) and pore volume (2.25 cm^3 g^{-1}). The obtained hierarchical porous carbons demonstrated remarkable capacitance of 240 F g^{-1}, energy density of 100 Wh kg^{-1}, and great cycle stability of 10% loss after 10000 cycles [116].

Briefly, chemical activation is a moderate temperature process and resulted to obtain high surface area ACs. However, repeatedly washing of ACs to remove inorganic and reactant residues is energy wasting and time consuming. Moreover, chemical activation leads to reduction of density and conductivity of the ACs and resulted in low energy density and performance. Therefore, to develop advanced materials for electrodes investigation on relationship of conductivity, porosity, and performance is necessary.
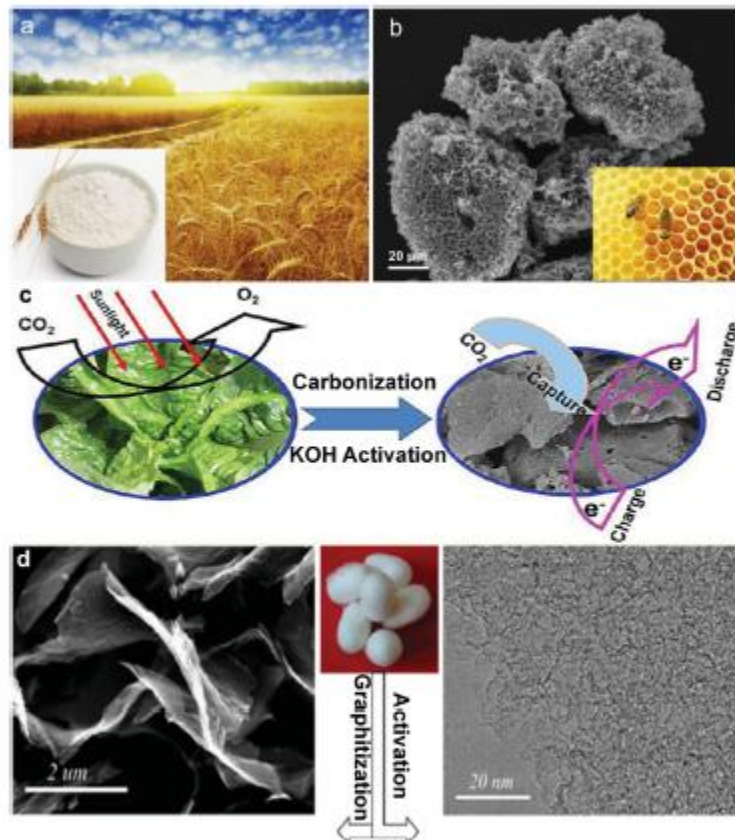
Figure 2.14: (a,b) Converting flour to carbon foam [84]. (c) Porous carbonaceous materials obtained from celtuce leaves [123]

2.7.3 HTC of Biomass Resources

Preparing nanostructured carbonaceous materials from natural resources (biomass) with controllable morphology and also modified surface can be reached by HTC

technique. While, using a sealed autoclave the aromaticity of structure of prepared carbon can be enhanced at low temperature (180-250°C). In addition, to improve the surface chemistry and area of obtained carbon materials, the HTC could be combined with chemical activation (addition of oxidizing agent). Different carbonaceous materials with excellent properties have been prepared from biomass resources for supercapacitor application, such as hemicellulose [126], D-glucosamine [109], fungus [127], microalgae [128], hemp [129], fungi [87], bamboo waste [130], and watermelon [131]. As an example, Sevilla et al. [128] reported synthesizing of microporous carbon materials from microalgae through combination of HTC process and chemical activation as shown in Figure 2.15. The obtained product exhibit remarkably high surface area ($\sim$2200m^2 g^{-1}) and acceptable electrochemical performance such as specific capacitance of $\sim$200 F g^{-1} and great rate capability (20% loose of capacitance at 20 Ag^{-1}). As shown in figure 7b, Wang et al. reported preparation of nanosheets carbons (graphene like) from hemp fiber through combined HTC and KOH activation, which represented high specific surface area ($\sim$2287m^2 g^{-1}) and excellent electrical conductivity around 226 Sm^{-1}.
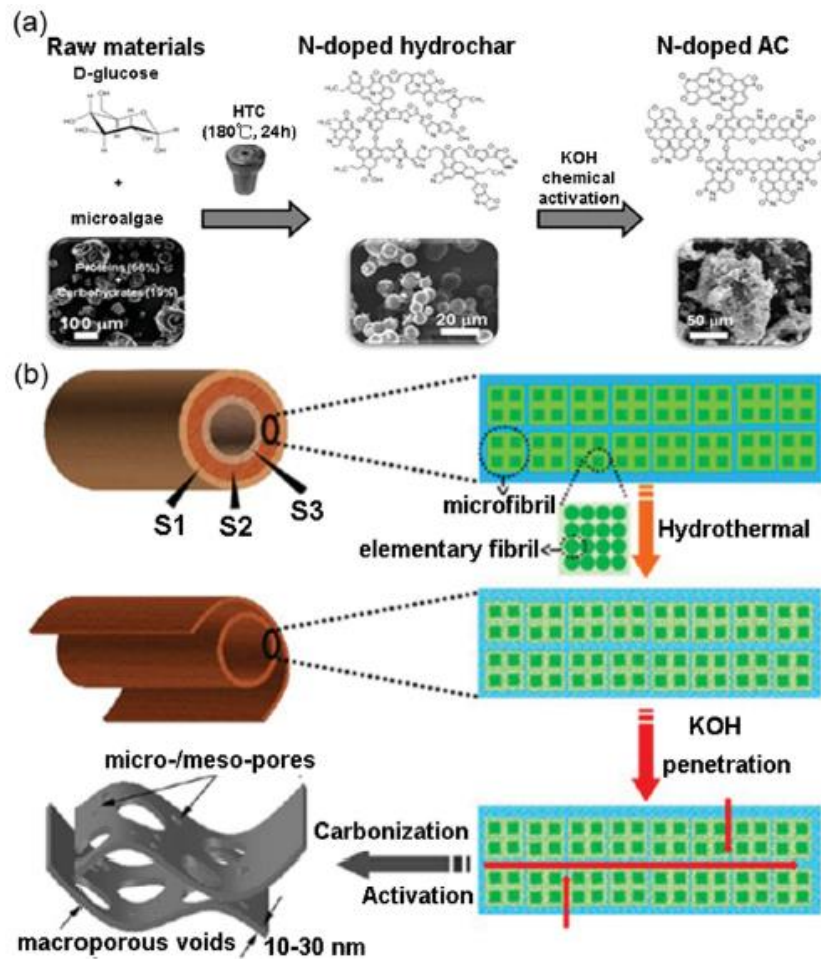
Figure 2.15: (a) Schematic of porous carbon preparation through KOH and HTc methodology from glucose and microalgae. (b) Schematic of preparation of carbon nanosheets from hemp [128]

2.8 Heteroatoms Presence in Carbon Framework as Pseudocapacitive Effect

Presence of heteroatoms such as nitrogen and oxygen in the carbon matrix leads remarkable capacitance enhancement due to various faradic reactions [132]–[141]. Additionally, the pseudocapacitive effect due to presence of heteroatoms assist EDL charging and also, they can be joined to suitable functional groups with fast faradic reactions. So, altering the gap between valence bands and conduction leads to valuable enhancement in adsorption of capacitive ions because of free electrons increase [33][142]. While using heteroatoms to enrich the carbon it should be considered that

the selecting of optimal doped material which depends on the polarity of electrode is necessary. For instance, redox pair of quinone-hydroquinone (oxygenated) play an important role in the cathode electrode (positive polarity) in acidic medium, while quaternary amines (nitrogen) is preferable for anode electrode (negative polarity) in alkaline medium [137]–[139].

2.8.1 Carbonaceous Materials Doped with Oxygen

Oxygenated functional groups present in carbon networks increase the capacitance properties of carbonaceous materials [137]–[139]. To obtain oxygen enriched carbons there are two main ways: (I) by selecting a precursor containing oxygen functionalities or (II) treatment of carbon material in a highly oxidative atmosphere. Carbonization of some biopolymers in one step like sodium alginate (SA) resulted in very interesting carbonaceous materials without any activation [137]. The structure of SA and cellulose are so close to each other but the thermal behavior of these two materials are so different. During the thermal treatment of cellulose at 400 ˚C decomposition is completed. While for SA at 700 and 900 ˚C weight loss happening due to the CO evolution. It is noteworthy that the obtained carbon material through pyrolysis of SA under argon flow at 600 ˚C is oxygen rich (15 at%) and microporous with specific surface area around 273 m^2g^{-1}. By deconvolution of XPS spectrum, the oxygen content is due to the ether and phenol groups (7.1 at%), quinone and keto groups (3.5 at%), and carboxylic groups (3.4 at%). Even the surface area of prepared carbon is low but its capacitance (200 Fg^{-1}, in 1 $molL^{-1}$ H_2SO_4) is comparable to the commercial activated carbons. On the cyclic voltammograms (three-electrode cell), the presence anodic and cathodic humps at 0.0 and -0.1 Vs $Hg/HgSO_4$ represent the pseudocapacitance contribution [137]. On the other hand, presence of peaks at same positions are due to the electrochemical reaction of oxygens of hydroquinone/quinone

pair of functional groups on the surface [143]. The high amount of capacitance for obtained carbon from SA is due to the charge transfer reactions on phenol, quinone, and ether groups [137]. Many researches have been conducted on carbonaceous materials obtained from seaweeds [138]. Some types of seaweeds represented acceptable capacitance properties after carbonization.

2.8.2 Carbonaceous Materials Doped with Nitrogen

Another heteroatom used as main dopant in carbonaceous materials is nitrogen. Nitrogen can be either substituted to carbon or used as functional groups such as polyaromatic structures as shown in Figure 2.16. Nitrogen doped carbonaceous materials can be prepared by carbonization of nitrogen containing polymers [132][133] or ammoxidation of carbons [141]. However, oxidative reactions occur in these kinds of procedures, oxygen also can be incorporated with nitrogen in carbonaceous network. Accordingly, capacitance measurement for only contribution of nitrogen is difficult. However, there is correlation between nitrogen content and capacitance of nitrogen doped carbonaceous materials obtained through carbonization of PAN or blend of pitch/PAN or polyvinylpyridine, following by activation (Figure 2.17). The prepared samples with specific surface area around 800 m^2g^{-1} showed proportional capacitance to the nitrogen content [132]. Such relationship reveals the crucial role of protons in pseudocapacitive mechanism.
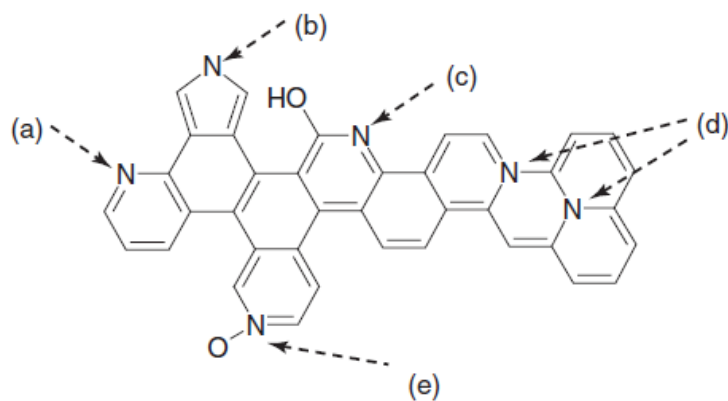
Figure 2.16: Various nitrogen functonalities in a carbon matrice
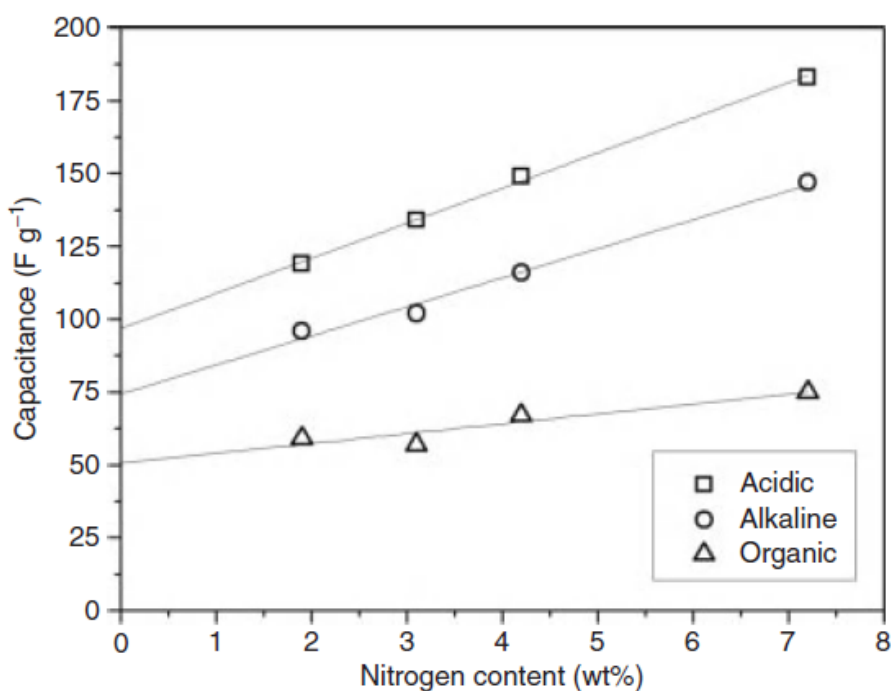
Figure 2.17: Capacitance amount Vs. nitrogen content of carbons in different electrolytes [132]

2.8.3 Carbonaceous Materials Doped with Boron

Boron among all those heteroatoms has been exhibited promising potent dopant to improve the electrochemical of carbon materials as electrode in supercapacitors. Boron atoms can be easily exchanged with carbon due to close atomic radius of carbon and boron. The charge transfer would be promoted by modification of electronic structure and carbon lattice [144]. Additionally, in carbonaceous materials doped with boron are

more eligible to attract OH⁻ ions from electrolyte because of electronegativity of born which is less than carbon and leads to improved conductivity [145]. Boron precursors mainly include H_3BO_3, B_2O_3, $KB(C_6H_5)4$, BF_3-MeOH, and $C_{16}mimBF_4$ [146]–[150]. Sahoo et al. reported preparation of boron doped graphene through hydrogen induced thermal reduction and H_3BO_3 which doped carbon exhibit remarkable discharge capacity of 548 m Ah g^{-1} due to the presence of boron and providing active sites [151]. The capacity of boron doped graphene comparing to the blank graphene increased by 1.7 times. Also, Jain et al. [152] prepared polyaniline/boron-doped graphene which exhibited a specific capacitance of 1134 F g^{-1} at 1 mV s^{-1} in 1 M H_2SO_4; and suggested that the boron-doped on the graphene introduced a P-type conductivity in the graphene which triggered a pseudocapacitive activity. The afore-mentioned studies demonstrate that heteroatom doping and the use of sucrose to prepare porous carbon is a cost-effective approach to develop electrode materials with tunable features for the fabrication of high-performance supercapacitors. Ling et al. [153] reported a sustainable and economic approach of recycling the boric acid template used as boron dopant source via evaporation crystallization. It shows that doping of materials by boron can be effective method to improve the electrochemical performance of electrode materials in supercapacitors application.

2.9 Artificial Neural Network (ANN)

There are different types of models to evaluate and study the supercapacitors performance [154][155]. The electrical and mathematical models are the best regarding to the performance report but at most cases are cumbersome [156]. According to the literature, limited studies are used ANN as a model to evaluate the performance of supercapacitors. Different subjects were evaluated employing ANNs due to their fascinated features such as easy to implementation, learning, and fast

computation. Some subjects which employed ANN are electronic industries, recognition of pattern, energy harvesting, medical application, chemical industries, etc [157]–[159].

One of the most developing areas of artificial intelligence is ANN which is also known as neural computing. Neural networks are consisting of some entities, which are known as neurons and operate in parallel mechanism. The origin of neural network is human nervous system [157].

Figure 2.18 shows the schematic of an ANN diagram. Where X represents the number of inputs which applied to the neuron ($X = (X_1, X_2,\ldots, X_n)$), Wi is weight of each input and b is the bias. Equation x represents the output of the neuron.

$$u = \sum_{i=0}^{n} WiXi - b \qquad\qquad (2.28)$$
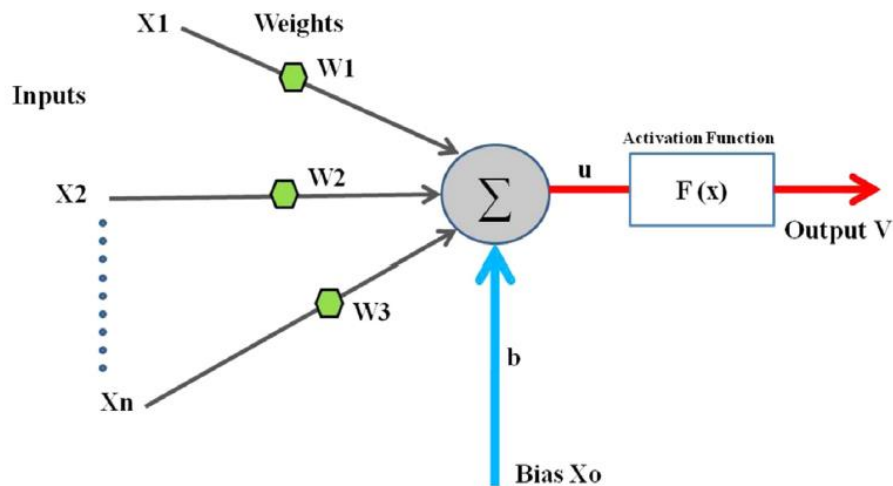
Figure 2.18: A model of Artificial Neural Network (ANN)

The neurons are linked together with connection link and a weight is given to each link that multiply to transmitted signal. An activation function (f(x)) is given to each neuron that assign the output. ANN mostly composed of three layers such as input, hidden,

and output layer as shown in Figure 2.19. So, ANN also well known as connection-oriented models [158].

Marie-Francoise et al. used ANN to evaluate electrical and thermal behavior of supercapacitors [160]. Wu C.H. et al. reported a developed model to predict the management and energy conversion of supercapacitor [161].
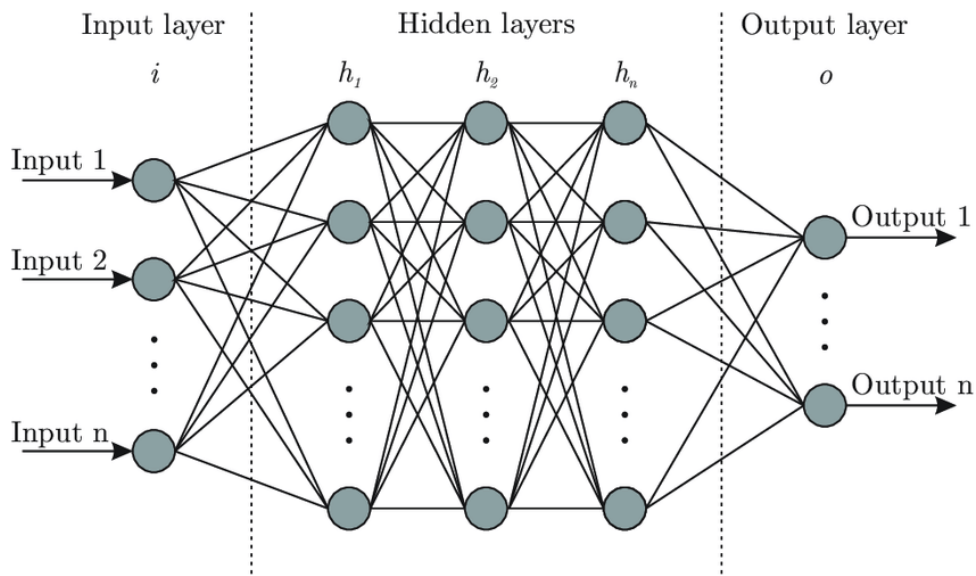
Figure 2.19: ANN different layers

Collectively, the performance of supercapacitor depends on the electrode materials, electrolyte pH, potential window and concentration of the dopants. It is worthy to state that, a significant number of researchers rely on several cumbersome empirical calculations or time-consuming trials to improve the capacitance of supercapacitors. In recent years, artificial neural network (ANN) modelling has been adopted as an effective and rapid technique to understand the complex and non-linear relationships between numerous variable input and output performance of a variety of systems [156][162]–[166].

Considering the complex variables in the development of high-performance supercapacitors, ANN modelling approach is considered suitable to establish the structure performance relationship. To date, ANN has attracted significant attention in pattern recognition, data analysis, medical diagnosis, waste generation and electronics industries [167][168]; however, the literature reports reveal that there are fewer initiatives undertaken for modelling supercapacitor performance by ANN.

Chapter 3

EXPERIMENTAL

3.1 Materials and Reagent

Analytical grade reagents were used without further purification and all the experiments were carried out under ambient conditions. Sulfuric acid (98% H_2SO_4), acetylene black (98.9 wt.%), polytetrafluoroethylene (PTFE 60 wt.%) as a binder, electrolytes (Na_2SO_4, H_2SO_4 and KOH), sucrose and boric acid were purchased from Sigma-Aldrich Co. Ltd (UK).

3.2 Preparation of Boron-Doped Porous Carbon Electrodes (B_x–pC)

Preparation procedures previously reported [105], [106] were modified to prepare B_x–pC samples. Typically, various mass fractions of sucrose and boric acid (4:0, 1, 2 and 3 wt.%) were mixed using an agate mortar and a pestle. Then, 5 mL sulfuric acid (1 M) was added to each mixture and stirred vigorously at 60 °C for 40 mins until homogeneous solutions were observed, note that highly exothermic reactions were noticed. After 10 mins, fluffy black materials obtained were collected and washed severally with deionized water to remove excess sulfuric acid and unreacted boric acid. Next, the samples were annealed at 50 °C for 24 h, and resulting solid products were carbonized at 800 °C under nitrogen flow at a heating rate of 10 $Cmin^{-1}$ for 60 min. Obtained boron-doped porous carbons are designated as B_x–pC (x represents the boron content).

3.3 Material Characterization

The samples morphologies were investigated using a scanning electron microscope (SEM, Zeiss LEO G34-Supra 35 VP, Germany). The samples were pretreated under vacuum at 130 °C for 3 h before analysis. Then, the Brunauer–Emmett–Teller (BET) specific surface area and pore size distribution were determined at − 196 °C using nitrogen adsorption–desorption isotherms measurements on Micrometics 3Flex surface Analyzer (Micromeritics Instrument Corp., USA). Information about electrode materials phase structure, thermal stability and material defect were identified using X-ray diffraction (XRD, Bruker D2 phaser, USA) with a monochromatic Cu Kα radiation (λ=1.5406 Å) at 40 kV and 30 mA; Shimadzu DTG-60H TGA machine (Japan) and Raman spectrometer (Renishaw PLC, England), respectively. Notably, all the characterizations have been done at Altinbas university.

3.4 Electrochemical Measurements

Initially, 2 g of slurries were prepared freshly (87 wt.% B_x–pC, 8 wt.% acetylene carbon black and 5 wt.% PTFE) in *N*-methylpyrrolidone. Certain weights of the as-prepared slurries were drop casted onto stainless steel substrates (1 cm^2), then, dried in a vacuum oven at 80 °C for 10 h. Typically, the active material mass loading of each working electrode is ~0.85 mg. To improve the strength, the composite electrodes were further thermally treated at 120 °C for 25 min. Electrochemical characterization was performed in a three−electrode system using cyclic voltammetry (CV) under different scan rates (5–100 mVs^{-1}) in a potential range of −0.7 to 0.3 V and galvanostatic charge/discharge cycling (0.2–20 A g^{-1}) using a CHI660 (Chenhua, Shanghai) workstation. The electrolytes used were 1 M H_2SO_4, 1 M Na_2SO_4 and 6 M KOH; graphite rod was used as a counter electrode, Hg/HgO as a reference electrode in KOH and Hg/Hg$_2$SO$_4$ as the reference electrode in H_2SO_4 and Na$_2$SO$_4$ at room temperature.

The impedance measurements were conducted with an alternate current amplitude of 5 mV in a frequency range of 100 kHz−0.1 Hz. All the working electrodes were soaked in the electrolytes for 2 h before each test.

The specific capacitance, C_{sp} of the supercapacitors were calculated from CV and galvanostatic charge–discharge curves (GCD) using Eqs.1 and 2 [152]:

$$C_{sp} = \int Idv/(vmV) \tag{3.1}$$

$$C_{sp} = I\Delta t/m(V_f - V_i) \tag{3.2}$$

As practical indicators, the specific energy density (E, Wh kg^{-1}) and power capability (P, W kg^{-1}) were calculated based on the obtained C_{sp}, following Eqs. 3 and 4 [162], [169], respectively:

$$E = C_{sp}V^2/2 \times 3.6 \tag{3.3}$$

$$P = E \times 3600/\Delta t \tag{3.4}$$

where I (mA) represents the response current; $\Delta V = V_f - V_i$: potential window; v: scan rate; m (mg): the mass of the electroactive materials; Δt: discharge time (s); V: the discharge voltage. Notably, electrochemical tests have been done at faculty of engineering, electrical engineering department, Altinbas university, Turkey.

3.5 Artificial Neural Network Modelling

An artificial neural network is a biologically inspired machine learning regression model with interconnected neurons often utilized for the description of complex non-linear relationships [156][162][170]. Doping heteroatom such as boron on the porous carbon may tune its electrochemical performance by acting as p-type trivalent impurities [153][171], while the presence of micropores and mesopores on the carbon materials may result in the formation of double-layer ion transport pathway, thereby increasing the supercapacitor capability [162]. We believe that ANN is suitable and

less cumbersome to analyze these complexities and relationships between these operating factors, electrode structural integrity and electrochemical performance of supercapacitor. The ANN architecture is designed to have an input layer (variables), one or several hidden layers and an output layer.

Here, our three-layered ANN architecture was built by combining an input layer with five variables, three hidden layers (11×7×3 interconnected structure) and a single output neuron as shown in Figure 3.1 using NeuroSolutions for MATLAB software (NeuroDimension, Inc. MA, USA). 95 experimental data sets were introduced into the ANN structure; to limit errors and improve convergence efficiency, inserted data were normalized in advance according to Eq.5 [165][167] to values within the range of 0 and 1. Then, the data sets were weighted and summed according to the Eq. 6 [162][163][165], then activated with l*ogsig* activation function and linear transfer function (purelin) at the hidden and output layers, respectively [170]. Eighty percent of input data was subjected to training, the trained subset was then evaluated by 10% validation subset, and the remaining subset was tested.

$$x_{nor} = x - x_{min}/x_{max} - x_{min} \tag{3.5}$$

$$z = b_{ji} + \sum_{j=1}^{n} w_j f\left(\sum_{i=1}^{m} W_{ji} x_i\right) \tag{3.6}$$

where x_{nor} is normalized variable, x_i, x_{min} and x_{min} are the input, minimum value, maximum value, respectively. Also, n, m are the input and hidden neurons; f represents the sigmoid activation function; w_j and W_{ji} are connection weights while b_{ji} is the bias associated with each layer, respectively. Eleven backpropagation algorithms were applied to train the network by adjusting the weights and bias; obtained results are tabulated.
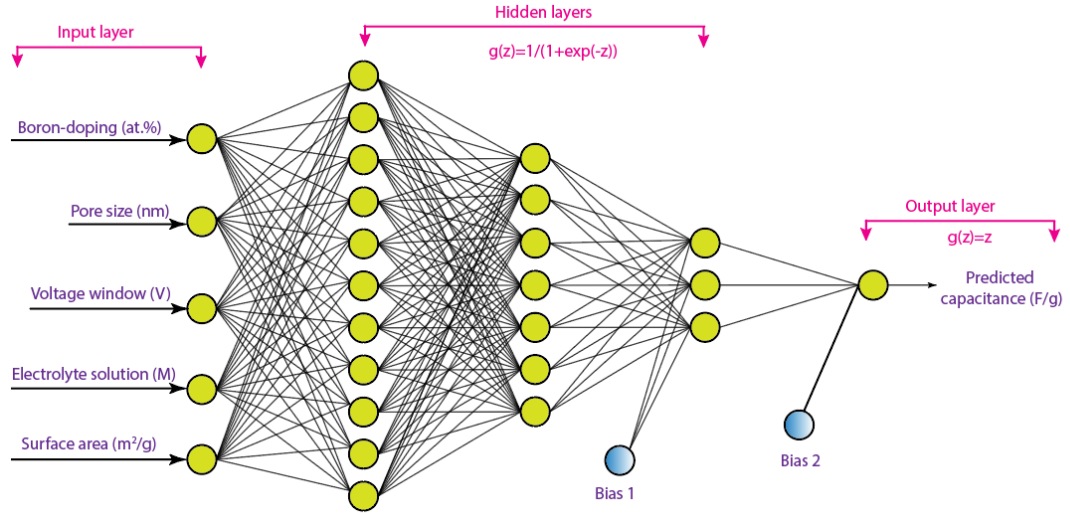
Figure 3.1: Optimized ANN architecture for prediction of capacitance of B_x–pC

As shown in Table 1, the Levenberg–Marquardt algorithm exhibited a very high degree of correlation (R^2=0.993) and least mean square error (MSE=0.00137); thus, was selected as the training algorithm to iterate the weights thousands of times. The relative significance of inputs in the validated ANN model to the output was calculated using the Garson equation:

$$I_j = \frac{\sum_{m=1}^{m=N_h}\left(\left(|W_{jm}^{ih}|/\sum_{k=1}^{Ni}|W_{km}^{ih}|\right)\times W_{mn}^{hz}\right)}{\sum_{k=1}^{k=Ni}\left(\sum_{m=1}^{m=N_h}(|W_{km}^{ih}|/\sum_{k=1}^{Ni}|W_{km}^{ih}|)\times W_{mn}^{hz}\right)} \tag{3.7}$$

Where I_j: relative importance of the input on the output; W: connection weights; N_h and N_i: represent numbers of hidden and input neurons; n, m, and k: output, hidden, and input neurons, and $i,\ h,\ z$: are the input, hidden and output layers, respectively.

Table 3.1: Comparison of training backpropagation algorithms for supercapacitor performance

Training algorithms	Epoch	MSE	Linear equations	R^2
Levenberg-Marquardt backpropagation	3400	0.00137	$y = 0.0562x + 0.0329$	0.993
Batch gradient descent with momentum	1100	0.03462	$y = 0.0089x + 0.0971$	0.786
Scaled conjugate gradient	950	0.05221	$y = 0.7659x + 0.0569$	0.489
Variable learning rate backpropagation	1200	0.00139	$y = 0.8761x + 0.0129$	0.599
BFGS quasi-Newton backpropagation	600	0.00248	$y = 0.5691x + 0.0067$	0.925
One step secant backpropagation	1100	0.00569	$y = 0.0549x + 0.0196$	0.897
Powell–Beale conjugate gradient	1000	0.04789	$y = 0.8965x + 0.0089$	0.986
Batch gradient descent	800	0.00133	$y = 0.4598x + 0.0339$	0.876

Polak–Ribiere conjugate gradient	900	0.00268	$y = 0.6799x + 0.0608$	0.907
Fletcher–Reeves conjugate gradient	1050	0.09873	$y = 0.0568x + 0.0419$	0.598
Resilient backpropagation	4000	0.01491	$y = 0.0009x + 0.0089$	0.899

The average number of iteration: 1463
The average time: 45.9 msec

Chapter 4

RESULTS AND DISCUSSION

4.1 Characterization Results

The nitrogen adsorption–desorption isotherms obtained for the carbonized sulfuric acid-pretreated sucrose is represented in Figure 4.1a. As observed, the plots demonstrated hybrid type I and IV isotherms according to the IUPAC classification [162][172]. Notably, all the isotherms exhibited very sharp knees at $P/P_0 = \sim 0.06$ and fairly flat plateaus until $P/P_0 = \sim 0.3$ suggesting the presence of a large number of micropores (< 2 nm); meanwhile, the hysteresis loops in relative pressure P/P_0 from 0.42 to 0.9 indicated narrow slit-shaped mesoporous (2–50 nm) [172]–[174] filling of the nitrogen gas which is pronounced in the B_2–pC sample.

Detailed pore size distributions analysis obtained using the density functional theory (DFT) method showed that the sucrose-based carbon materials exhibited interconnected pore structures as shown in Figure 4.1b. It can be observed that the undoped carbon material (B_0–pC) displayed pore size mainly in the micropore region with an obvious peak at 0.85 nm. Both B_1–pC and B_4–pC exhibited a bi-modal micropore distribution with an average pore size of $\sim$1.65–1.89 nm. B_2–pC and B_3–pC, on the other hand, have tri-modal pore distribution structures with a wide range from 0.93 to 2.88 nm. While the existence of micropore is critical for capacitance enhancement [171][174][175], the higher proportion of mesopores exhibited by B_2–pC compared to others serves as ion diffusion routes to the internal surface of the

electrode material and active sites for charge storage which is beneficial for high capacitive performance [162][175].
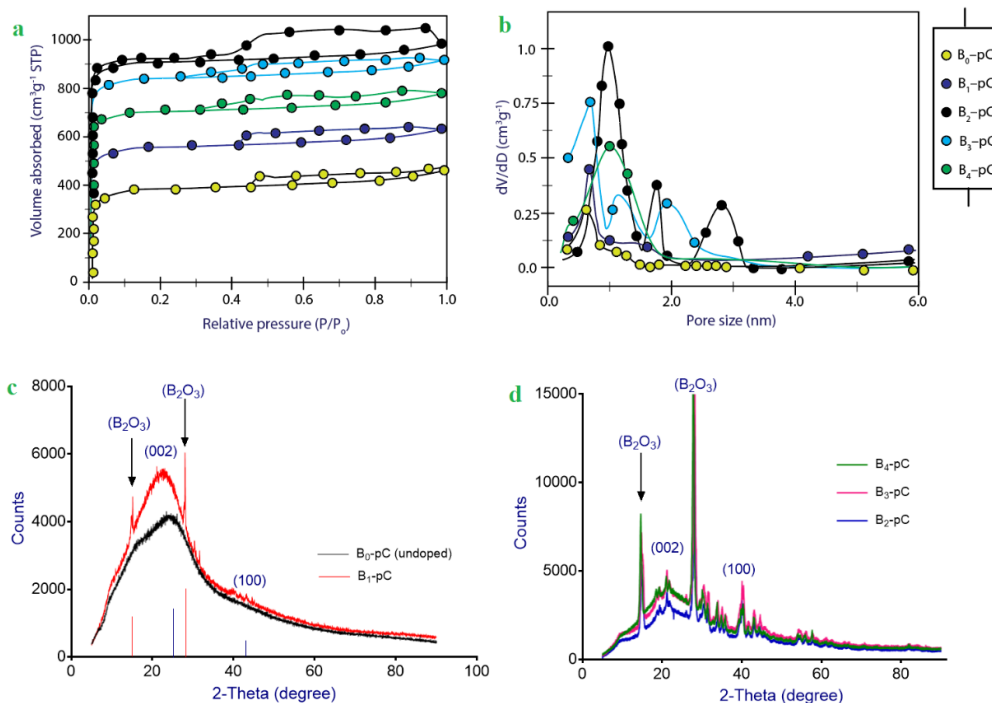
Figure 4.1: (a) Nitrogen adsorption–desorption isotherms (b) Pore-size distribution and (c and d) X-ray diffraction patterns of B_x–pC samples

The surface characteristics of the as-fabricated porous carbons are listed in Table 4.1. Note that the specific surface area increased significantly from 388.7 m^2g^{-1} for undoped porous carbon material B_0–pC to 1298.9 m^2g^{-1} for B_2–pC (containing 2 wt.% boron), suggesting that boric acid contributed to the surface area enhancement. Even though the exact mechanism is unknown, the boric acid can enter the internal space of the sucrose and initiate the expansion of the internal structure. Similarly, Li et al. [176] reported that boric acid increased the BET specific surface area of graphene aerogels and concluded that with B atoms, the doped graphene possesses a larger specific surface area.

However, the surface areas and mesopore volumes of the samples decreased as the boron doping increased; suggesting that excessive boron content led to agglomeration and decreases in the pore volumes and surface area. Similarly, Shang et al. [171] reported that excessive melamine doping (nitrogen source) on Houttuynia-derived porous carbon caused the collapse of significant amounts of pores on the carbon material and negatively affected the performance of the electrode material.

The XRD patterns of the electrode materials are given in Figure 4.1 c-d. For all B_x–pC; broad diffraction peaks centred at ~22° attributed to (002) interlayer spacing (~3.56 nm) of disordered carbon and weak signals at ~43° assigned to (100) 1.89 nm plane of graphitized carbon were observed. Moreover, the boron-doped carbon samples (B_1–pC to B_4–pC) present pronounced peaks from boron oxide with the formation of more graphitic porous carbon materials which is consistent with boron-doped biomass-derived carbon nanosheets reported by Ling et al. [153]. Also, the (002) diffraction peaks of boron-doped samples shifted slightly towards the left, suggesting increased defects with the introduction of heteroatom into the carbon structure.

Morphology information obtained via SEM is presented in Figure 4.2. The undoped carbon (B_0–pC) shows a rough spongy-like structure with few visible pores distributed on its surface (Figure 4.2a). In comparison, widened hierarchical cluster of pores are visible on the surface of the boron-doped carbon samples (B_1–pC to B_3–pC); while excessive boron content was believed to collapse the pores in B_4–pC which exhibited chunky morphology. Among the boron-doped samples, the B_4–pC has the lowest total pore volume according to Table 4.1 results which is consistent with the SEM analysis.

The photographs of the boron-doped sulphuric acid pre-treated sucrose carbons are presented in Figure 4.2f.
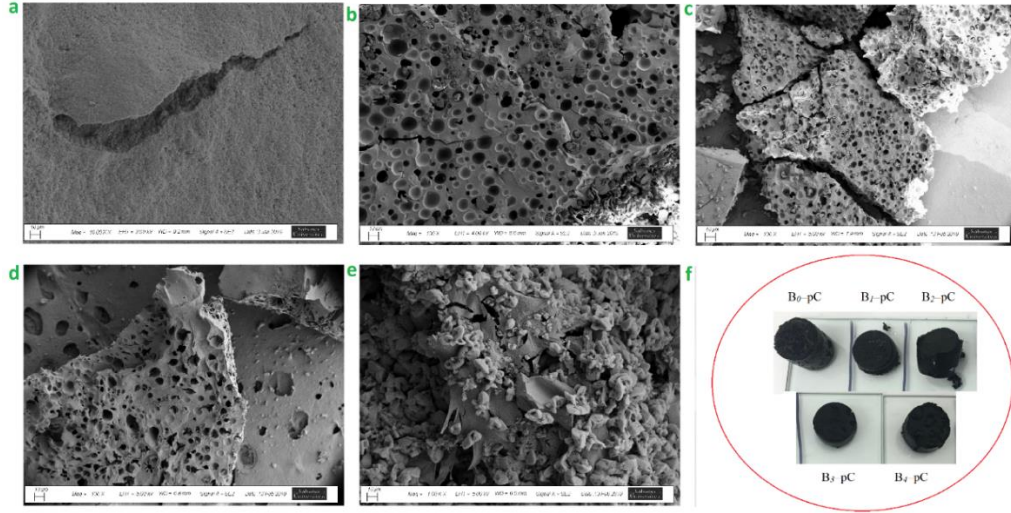
Figure 4.2: SEM images of (a) Undoped sucrose-based carbon (B_0–pC) (b) B_1–pC (c) B_2–pC (d) B_3–pC (e) B_4–pC and (f) Optical images of doped and undoped porous carbon samples

Table 4.1: Specific surface area and pore structure parameters of B_x–pC materials

Samples	SSA (m^2g^{-1})	V_t ($cm^3 g^{-1}$)	V_{mes} ($cm^3 g^{-1}$)	V_{mic} ($cm^3 g^{-1}$)	V_{mes} /V_t (%)	P_{BJH} (nm)
B_0–pC	388.7	0.58	0.17	0.41	29.3	1.39
B_1–pC	745.9	1.02	0.45	0.57	44.1	1.65
B_2–pC	1298.9	2.11	1.42	0.69	67.2	2.88
B_3–pC	879.8	1.79	1.13	0.66	63.1	2.45
B_4–pC	1098.7	0.98	0.35	0.63	35.7	1.89

V_t: Total pore volume.
V_{mes}: Mesopore volume.
V_{mic}: Micropore volume obtained from the Dubinin–Radushkevich eqn.
P_{BJH} (nm): Average pore diameter calculated from the desorption data by Brunauer–Joyner–Halenda eqn.

Raman spectroscopic tool was employed to characterize the type of carbon structures, graphitization degree and disordered structures in the B_x–pC samples. Figure 4.3a shows two characteristic peaks in all the samples; the D band centred at 1342 cm^{-1} reveals sp^3 imperfect and disordered graphitic lattice while the G band at 1582 cm^{-1} corresponds to sp^2 graphitic lattice of carbon [106][162][171]. The intensity ratio between the two bands (I_D/I_G) reveals the degree of imperfection in the samples, a small I_D/I_G intensity ratio indicates small amounts of efects [105][153][162][177]. According to Zhou et al. [105], the heteroatom doping such as B can increase the defects in the materials which results in amorphization of the graphitic carbon. The B_0–pC, B_1–pC, B_2–pC, B_3–pC and B_4–pC shows I_D/I_G of 1.31, 1.03, 0.97, 1.29, and 1.18, respectively, revealing the existence of both ordered graphite and disordered amorphous structures in the samples. Notably, the B_2–pC exhibited the lowest I_D/I_G which suggests it exhibited the greatest graphitic behavior [176].
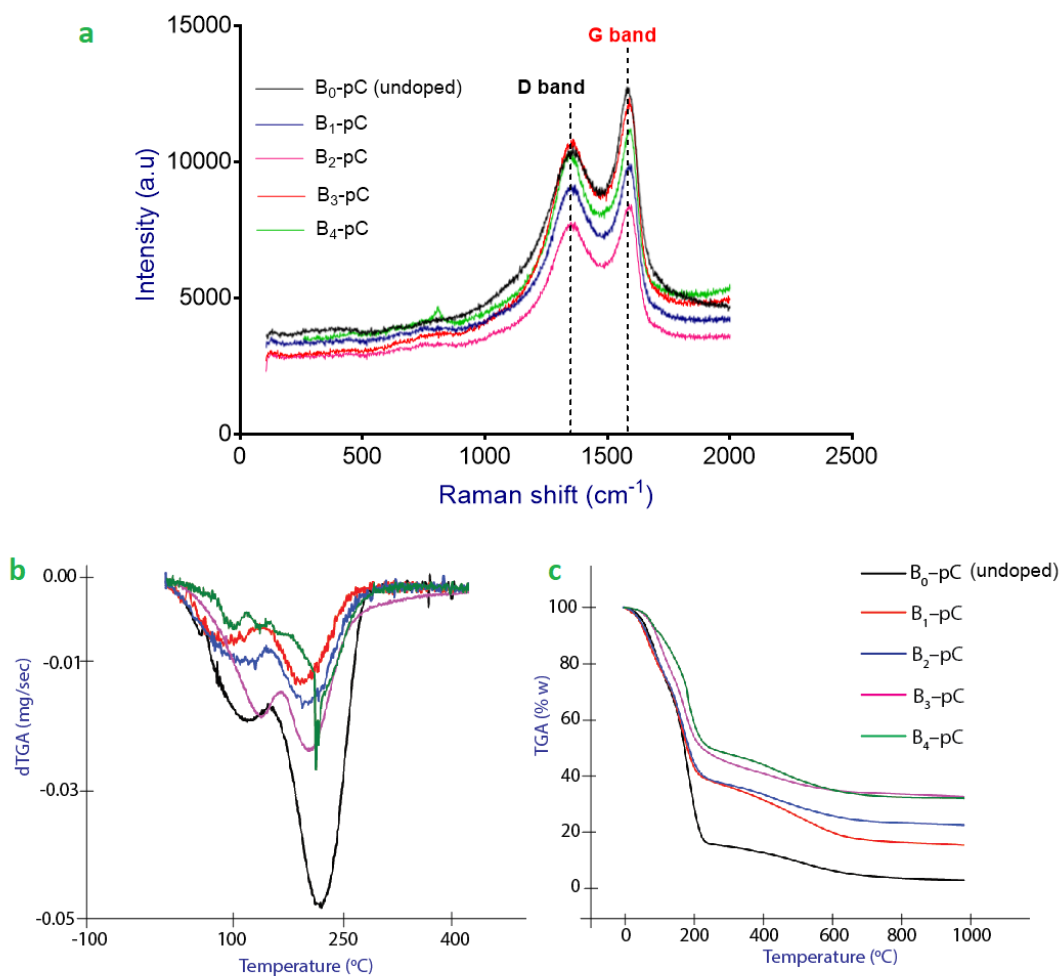
Figure 4.3: (a) Raman spectra (b) dTGA curves and (c) TGA curves of B_x–pC samples

Figure 4.3b-c represents the differential thermal gravimetric analysis (DTG/TGA) of the samples. The weight losses at ~120 °C for all the samples are related to the desorption of physically adsorbed moisture. It is obvious that B_0–pC exhibited the highest weight loss at ~120 °C, this is probably due to its high amorphous nature revealed in the XRD and Raman spectra results. While the lower weight losses for samples B_1–pC and B_4–pC compared with B_2–pC may be attributed to their lower surface areas [106]. The obvious weight loss observed at 235 °C is ascribed to the combustion of the amorphous carbon in the samples, beyond this, the mass of the samples was relatively stable until ~658 °C which is related to change in the degree of

graphitization of the samples. In total, 59, 39, 23, 16, 15% weight loss were observed for B_0–pC, B_1–pC, B_2–pC, B_3–pC and B_4–pC, respectively. Guo et al. [106] observed similar weight loss pattern when they subjected sucrose-based microporous carbons to heat treatment.

4.2 Electrochemical Performance of B_x–pC Based Electrode Materials

The capacitive performance of B_x–pC based electrode materials was investigated by CV, GCD and EIS techniques in acidic, basic and neutral electrolytes using a three-electrode system. Note that to avoid the oxidation of the carbon materials in the acidic (H_2SO_4) electrolyte, we adopted a partial negative voltage from -0.7 to 0.3 V. Fig.5a$-$c shows the CV curves of B_x–pC electrodes at a scan rate of 5 mVs^{-1}. Except for the B_0–pC, they all exhibit nearly symmetrical rectangular-like shape along with slight humps, redox peaks noticeable around -0.2 V (vs Hg/Hg_2SO_4). As previously reported, these deformations (redox peaks) are a characteristic feature of faradic reactions caused by electrochemically active functionalities such as B/N/P/O heteroatoms [153][178][179]. Considering the shape and slight distortions, the capacitive behaviour of the B_x–pC electrodes is a combination of double-layer capacitances and pseudocapacitance due to heteroatom in the carbon moiety.
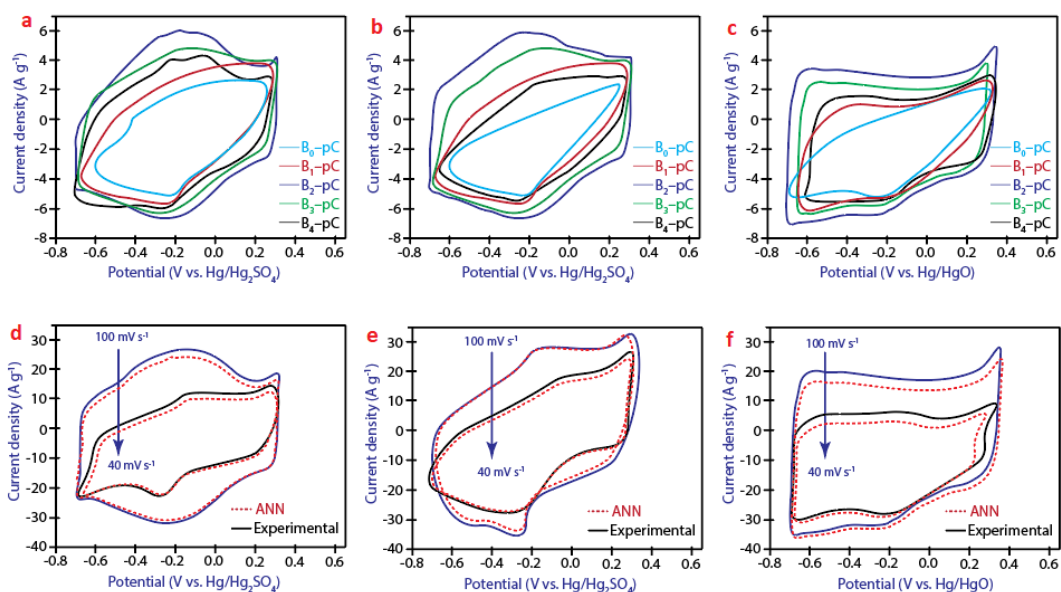
Figure 4.4: CV curves of B_x–pC electrodes at scan rate of 5 mV s^{-1} in (a) 1 M Na$_2$SO$_4$ (b) 1 M H$_2$SO$_4$ (c) 6 M KOH; and CV curves of B_2–pC electrodes at scan rate of 40 mV s^{-1} (black color) and 100 mV s^{-1} (blue color) in (d) 1 M Na$_2$SO$_4$ (e) 1 M H$_2$SO$_4$ (f) 6 M KOH

As can be seen from the cyclic voltammograms in the different electrolyte (Figure 4.4a−c), both H$_2$SO$_4$ and Na$_2$SO$_4$ produce an almost similar shape while KOH reflected a slightly different quasi-capacitive shape. The highest specific capacitance was achieved in the H$_2$SO$_4$ medium (Figure 4.4b) which is attributed to its higher ionic conductivity and faster H$^+$ (2.80 Å) mobility in comparison to K$^+$ (3.31 Å) and Na$^+$ (3.58 Å), and consistent with another report [179]. By comparison, the CV curve of B$_2$–pC exhibited the largest encircled loop, indicating the largest capacitance among all the electrodes which is attributed to its obvious interconnected honeycomb-like porous structure, high specific surface area (1298.9 m^{2}g^{-1}) and higher proportions of mesopores. The CVs of B$_2$–pC at scan rate 40 and 100 mVs^{-1} in the different electrolyte is shown in Figure 4.4d−f. It is noted that even at a high potential scan rate of 100 mVs^{-1}, B$_2$–pC still presented a nearly quasi-rectangular shape indicating its good rate performance; although with obvious distortions in the H$_2$SO$_4$.

GCD curves of B_x–pC at the current density of 0.2 A g^{-1} is presented Figure 4.5a−c. The curves exhibited obvious quasi-triangle shapes rather than a nearly symmetrical triangle (notably in the acidic and neutral electrolyte), attributed to the pseudocapacitance contribution from the B heteroatom in the carbon frameworks [179][180]. In the 6 M KOH, B_x–pC revealed more of a typical double-layer capacitor behaviour and excellent electrochemical reversibility. B_2–pC presented the largest discharging times, indicating the largest specific capacitance. The results are consistent with those of CV scans. Furthermore, the GCD curves of B_2–pC was examined at different current densities (0.2–10 A g^{-1}).

As shown in Figure 4.5d−e, B_2–pC maintained the quasi-triangle shape well even at high current densities with small internal resistance, which is probably due to its higher proportion of mesopores [171] and pseudocapacitance provided by sufficient B heteroatom. At 0.2 A g^{-1}, B_2–pC showed specific capacitance of 351 F g^{-1} which is higher than 196 F g^{-1} and 238 F g^{-1} for B_0–pC and B_4–pC, respectively (Figure 4.5f). The trend reveals that doping sufficient B (2 at. %) on the carbon drastically improved the specific capacitance by pseudo-capacitance reaction while excess boron (4 wt.%) limited charge distribution on the carbon frameworks. Note that the specific capacitance of B_x–pC decreased steadily as current density increased suggesting limited electrolyte ion diffusion into the core structure of the active materials, hence, redox reactions do not have enough time to occur at high current densities [105][181].
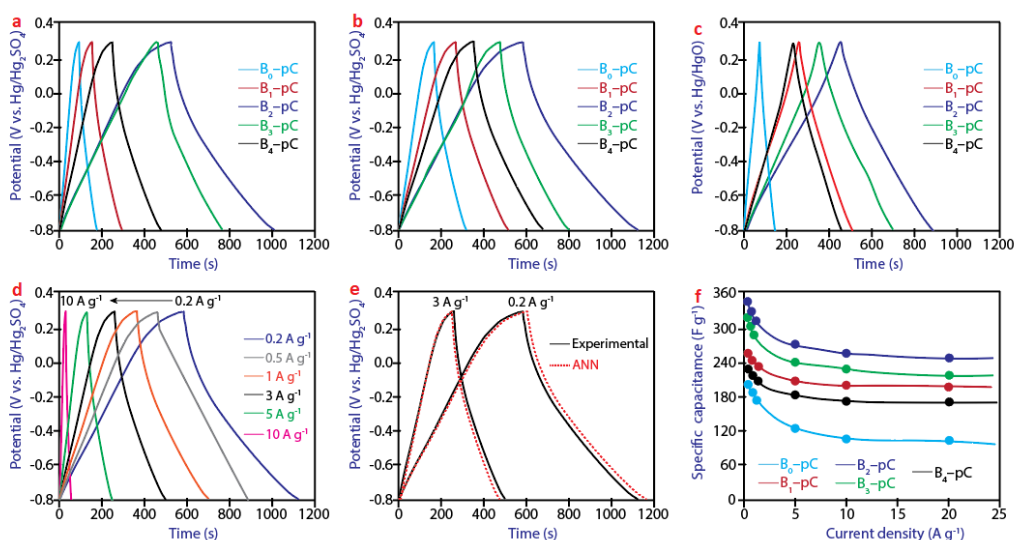
Figure 4.5: Galvanostatic charge–discharge curves of B_x–pC electrodes in (a) 1 M Na_2SO_4 (b) 1 M H_2SO_4 (c) 6 M KOH; and (d) GCD curves of B_2–pC electrodes at current density of 0.2–10 A g^{-1} (e) Experimental and ANN predicted GCD curves of B_2–pC at 0.2 and 3 A g^{-1} (f) Specific capacitance of B_x–pC at current density of 0.2–20 A g^{-1}

Findings from the GCD and CV were confirmed by the EIS and presented in Figure 4.6a−c. The Nyquist plots of B_x–pC exhibited typical features of porous electrodes with semicircles at high-frequency, nearly vertical lines at the low-frequency region and ~45° sloped Warburg impedance at the medium frequency [105][171]. The intercept on the real axis (Z') represents the electrode resistance [182]. Considering the curves in Figure 4.6a, all samples exhibited low electrode resistance (R_e) of ~0.2 Ω cm^2. The semicircles represent the bulk electrolyte resistance (R_∞), which contributed majorly to the internal resistance. B_2–pC exhibited the lowest internal resistance ($R_e + R_\infty$) of 1.3 Ωccm^2 which is lower than 1.68 Ω cm^2 internal resistance exhibited by B_0–pC (Figure 4.6b). This is attributed to the sufficient proportion of micro-/mesopores, higher specific surface area and the improved surface wettability of B_0–pC after boron doping. Also, among all the samples, B_2–pC exhibited the lowest diffuse layer resistance at the low-frequency region, revealing its excellent capacitive characteristic, lowest ion diffusion route and superior conductivity.

As presented in Figure 4.6c, the bulk electrolyte resistance of B_2–pC increased from 1.1 Ω cm^2 to 1.58 Ω cm^2 after 2000 cycles, which is likely due to the corrosion of the collector and loss of adhesion of active material from the current collector [183]. The results of cycling performance tests of the B_2–pC electrode and its symmetric supercapacitor (B_2–pC//B_2–pC) are presented in Figure 4.6d. As seen, the symmetric supercapacitor maintained capacitance retention ~98.9% after 2500 cycles at 1 A g^{-1} for 1.0 V. Similarly, the B_2–pC electrode maintained ~98.5% of its initial capacitance where its specific capacitance reduced from 312.3 to 307.6 F g^{-1} after 2500 cycles. The results herein suggest that the boron-doped sucrose porous electrodes have excellent capacitance retention and long life stability. Note that, the B_2–pC electrode exhibited comparable cycling performance with various other porous carbon-based electrodes in the literature [14][106]–[108][171]. However, its retention capacity is higher than V_2O_5-based electrode material that has maximum capacity retention of 71% after 1000 cycles [184].

The CV studies of B_2–pC//B_2–pC symmetric cell were performed at different potential windows from 0.8 to 1.4 V in 1 M H_2SO_4 aqueous electrolyte at 30 mV s^{-1}. The loops exhibited rectangular-like shapes without noticeable enhancement in the anodic current even at 1.3 V as shown in Figure 4.6e, revealing excellent reversibility and ideal EDLC behaviour [105][162]. Meanwhile, the anodic current increased obviously when the potential was extended further to 1.4 V, attributed to the decomposition of the electrolyte. Note that the wide voltage window of 0–1.3 V may be attributed to the honeycomb-like interconnected porous structure of the B-doped carbon material which provided an effective route for faster H^+ mobility [180].

The power density and energy density of the symmetric and asymmetric supercapacitors were calculated and obtained Ragone plot is presented in Figure 4.6f. From the Ragone plot, the B_2–pC//B_2–pC, B_0–pC//B_0–pC and B_2–pC//B_0–pC retained maximum energy density of 27.67, 20.45 and 6.98 Wh kg^{-1}, respectively at 3.0 Ag^{-1}. The value of B_2–pC//B_2–pC is slightly higher than that of the asymmetric B_2–pC//B_0–pC but remarkably higher than the symmetric B_0–pC//B_0–pC. It is worth noting that the B_2–pC//B_2–pC supercapacitor could attain a high power density of 3900 W kg^{-1} at the maximum energy density. The boron dopant in B_2–pC enhanced its specific capacitance as a result of the pseudocapacitive effect, and the interconnected micro-/mesopores improved its energy storage mechanism compared to the B_0–pC//B_0–pC. Interestingly, the maximum energy density achieved by the symmetric B_2–pC//B_2–pC supercapacitor is superior or comparable to the recently reported carbon-based and MnO_2-based asymmetric supercapacitors [105][162][174][183].
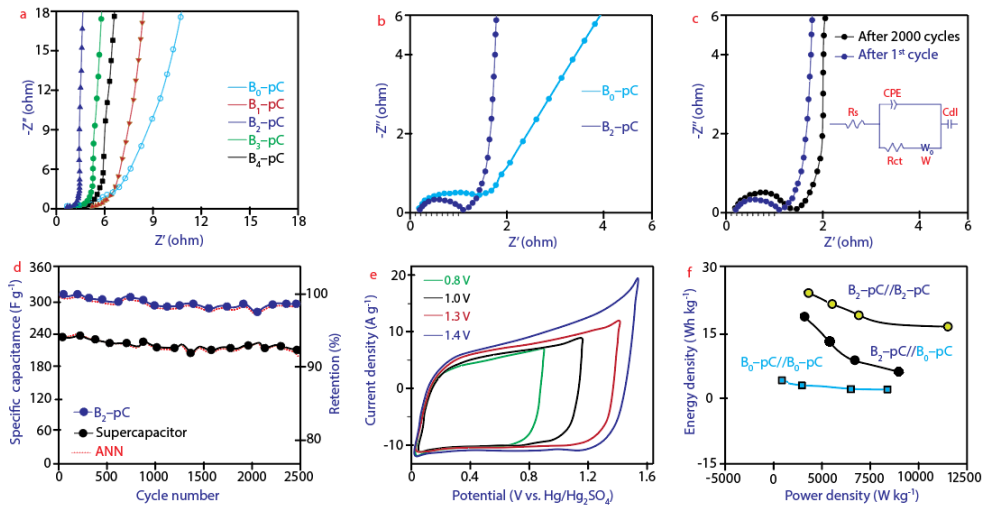
Figure 4.6: Nyquist plots of (a) B_x–pC (b) B_0–pC and B_2–pC (c) B_2–pC in 1 M H_2SO_4 electrolyte solutions (inset: electrical equivalent circuit) (d) Cyclic stability of B_2–pC and its symmetric supercapacitor 1 M H_2SO_4 (e) CV curves of B_2–pC in 1 M H_2SO_4 at 30 mV s^{-1} within different voltage windows (f) Ragone plots

4.3 Analysis of the ANN Model

The operational conditions (voltage window, nature of the electrolyte, size of collectors) and structural parameters of electrode materials have a strong relationship with the performance of supercapacitors. Presently, no accepted theoretical models or empirical strategy to systematically enhance the capacitance of a supercapacitor. To solve this problem, we applied artificial intelligence modelling (ANN) herein to discover relationships between operational and electrode parameter inputs and specific capacitance outputs of the electrode and symmetric B_2–pC//B_2–pC supercapacitor. B_2–pC was selected considering its performance as compared with other symmetric B_x–pC materials.

The ANN architecture is shown in Figure 4.7 and parameters of the optimized ANN model used here is presented in Table 3. Note that in the training and testing sets, the least mean square error (MSE) and the highest value of the correlation coefficient (R^2) were adopted as a yardstick. Hence, when 21 neurons were used in the hidden layers, the MSE reached the lowest level; but increasing the number of neurons beyond 21 failed to decrease the MSE further. Thus, 21 neurons were selected to develop the ANN topology shown in Figure 4.7.
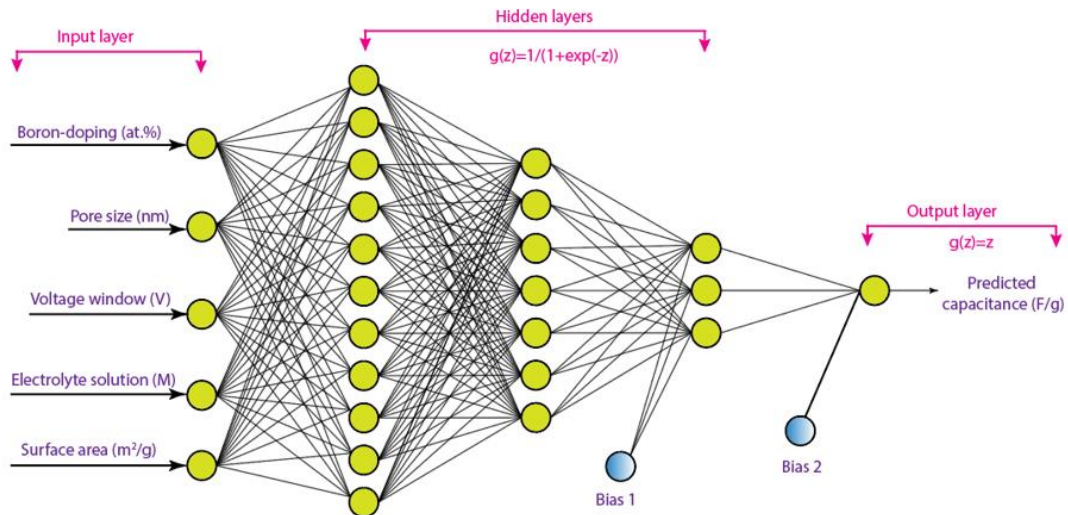
Figure 4.7: Optimized ANN architecture for prediction of capacitance of B$_x$–pC

Table 4.2: Parameters of the optimized ANN and optimization of hidden layer neurons

Parameter	Value	Input layer	
		Parameter	Range
Training method	Levenberg–Marquardt backpropagation	Boron-doping (at.%)	0–4
Transfer function of hidden layer	*Logsig*	Pore size (nm)	0.8–3.0
Error goal	0.012%	Voltage window (V)	0.4–2.0
Learning rate	0.3	Surface area (m^2 g^{-1})	300–1400
Momentum (mu)	0.001	Electrolyte solution (M)	1 M H$_2$SO$_4$, 1 M Na$_2$SO$_4$ and 6M KOH
Data division	Random		
Epochs	3400		
Input layer neurons	5		
Hidden layers	3		
Hidden layer neurons	21		
Output layer neurons	1		
Bias	2		

Optimization of hidden layers' neurons

No. of Neurons	Training set		Testing Set	
	MSE	R^2	MSE	R^2
18	0.0939	0.8991	0.1284	0.7895
19	0.0689	0.9359	0.1459	0.8913
20	0.0443	0.9598	0.0123	0.9108
21	**0.0214**	**0.9995**	**0.0089**	**0.9349**
22	0.0218	0.9867	0.0089	0.9056
23	0.0228	0.9908	0.0198	0.9008

$$MSE = 1/n \sum_{i=1}^{n} (Y_i - Z_i)^2$$: n number of predictions on all variables, Y_i observed values and Z_i is predicted values.

Bold: optimum number of hidden layer neuron with least R^2 and MSE

We adopted the ANN to establish the relationships between the input parameters and output of the assembled symmetric supercapacitors since its correlation (R^2= ~0.992 and 0.9098) is nearly 1 for training and validation data of the electrodes, respectively as shown in Figure 4.8a–c. As shown in Figure.8c, B_2–pC//B_2–pC containing 2 wt.% boron exhibited the highest specific capacitance (238.5 F g^{-1}) in 1 M H_2SO_4 at 1 A g^{-1} compared to 233.6 and 176.9 F g^{-1} in 1 M Na_2SO_4 and 6 M KOH; the ANN predicted values are consistent with the observed values. The higher specific capacitance achieved with the acidic electrolyte as opposed to the neutral and basic electrolyte is probably due to the greater conductivity and faster mobility of H^+ compared to Na^+ and K^+ [179].

Considering the randomness nature of ANN, we run the optimum ANN topology herein for 9 times to establish the stability of the prediction values. As presented shown in Figure 4.8e, the average predicted specific capacitance is 246.3 F g^{-1}, which is nearly close to the actual specific capacitance of 238.5 F g^{-1}. Also, the obtained desirability function of 0.93 which is closer to 1.0 suggests that the ANN model herein can represent the observed scenario, simulate and predict the relationships between the output of a supercapacitor and the complex independent variables. We employed a random forest algorithm and Garson equation (Eqn.7) to investigate the relative importance of each input. As represented in Fig.8d, the electrode specific surface area, heteroatom (boron) doping and nature of electrolyte used account for 89.8% in the ANN prediction model.

Notably, the specific surface area accounts for the largest proportion (40.5%) which is reasonably consistent with other experimental reports [156][162]. Wang et al. [162] modelled the performance of algae-based active carbon supercapacitors using 10

independent variables via an artificial neural network and reported that specific surface area contributed 30.1% in the ANN prediction which is the largest feature. A high specific surface area enables the electrode material to store more charge by providing sufficient contact area to absorb electrolyte ions [162]. The pore size contributed 6.6% in the ANN prediction; generally, electrode materials with high total pore volume exhibit better performance as ion transport routes or reservoir during charging and discharging process [14][152][162][183][185]–[187].

Table 4.3: Comparative performance of reported carbon materials for supercapacitor

Materials	Dopant	SSA (m^2g^{-1})	Electrolyte	Scan rate	C_{sp} $(F\ g^{-1})$	Refs.
B/N co-doped carbon powder	B/Nitrogen	416	1 M H_2SO_4	0.1 A g^{-1}	358	[11]
B/N co-doped carbon film	B/Nitrogen	416	6 M KOH	100 A g^{-1}	140	[11]
B/N co-doped carbon	B/Nitrogen	894	6 M KOH	0.1 A g^{-1}	268	[39]
Sucrose-based carbon	–	603.4	30 wt.% KOH	0.1 A g^{-1}	232.6	[15]
N-doped porous carbon	Nitrogen	1751	6 M KOH	1 A g^{-1}	335	[12]
N-doped porous carbon	Nitrogen	2563.3	6 M KOH	1 A g^{-1}	251.4	[3]
N-doped carbon spheres	Nitrogen	213	6 M KOH	0.5 A g^{-1}	213	[40]
Sucrose-based activated carbon	Nitrogen/O	518	1 M H_2SO_4	0.5 A g^{-1}	277	[17]
B_2–pC	Boron	1298.9	1 M H_2SO_4	1 A g^{-1}	312.3	This study
B_2–pC	Boron	1298.9	1 M Na_2SO_4	1 A g^{-1}	298.8	This study
B_2–pC	Boron	1298.9	6 M KOH	1 A g^{-1}	275.7	This study
B_0–pC	–	388.7	1 M H_2SO_4	1 A g^{-1}	178.6	This study

Actual and ANN predicted performances of B_2–pC//B_2–pC symmetric supercapacitor

Current density $(A\ g^{-1})$	Discharge time (s)	C_{sp} $(F\ g^{-1})$		E (Wh kg^{-1})		P (W kg^{-1})	
		Actual	ANN	Actual	ANN	Actual	ANN
0.2	972.96	299.37	287.67	70.27	72.34	260.02	265.24
0.5	345.82	266.02	272.45	62.44	60.89	650.11	656.88
1.0	155.05	238.54	246.31	55.99	59.37	1300.03	1289
3.0	25.54	117.88	113.59	27.67	29.19	3900	3909.2
5.0	9.89	76.08	82.11	17.86	16.95	6500	6498.9

Active electrode mass is 0.85 mg
Active potential window, ΔV is 1.3V
The electrolyte is 1 M H_2SO_4
B_2–pC: Boron-doped sucrose
B_0–pC: un-doped sucrose
SSA: Specific surface area

The Nyquist plots (Fig.8f) of the symmetric B_2–pC//B_2–pC using different electrolyte further revealed that the supercapacitor exhibited the lowest internal resistance (R_e=a

(electrode resistance) and $R_\infty = b$ (bulk electrolyte resistance)) in the acidic electrolyte which is represented also by the CV and GCD results. B_2–pC exhibited considerably high specific capacitance which is much better than the other B_x–pC electrode materials and recently reported nitrogen/boron doped-carbon materials as demonstrated in Table 4.3. This could be as a result of its well-developed micro-/mesopores with the average pore size of 28.8 Å, respectively, which is significantly larger than the radii of the solvated electrolyte cations and anions ($Na^+ \approx K^+ = 3.6$–3.3 Å $> H^+$ (2.8 Å) and SO_4^{2-} (3.8 Å) $> OH^-$ (3.0 Å)) [185][188]. Hence, these dissolved ions conveniently entered the widened pores and formed electrical double layers; while the boron dopant enhanced the wettability of the carbon by modifying its polarity.
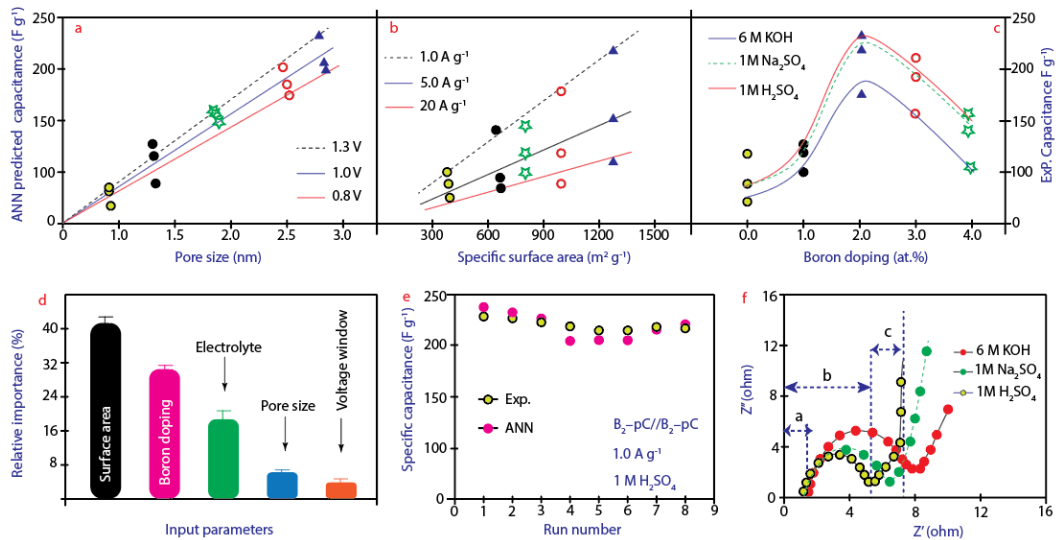
Figure 4.8: Relationship between capacitance and (a) Calculated pore size (b) Specific surface area (c) B-doping amount (d) Relative importance of variable input parameters to output (e) Actual specific capacitance of B_2–pC//B_2–pC and ANN predicted for nine times (f) EIS of B_2–pC//B_2–pC in different aqueous electrolytes (a: electrode resistance; b: internal resistance; c: diffuse layer resistance)

Chapter 5

CONCLUSION

We have developed a facile strategy for the production of B-doped sucrose carbon (B_x–pC) using sulfuric acid and boric acid followed by carbonization. B_x–pC exhibited sufficiently high specific surface areas (745.9 −1298.7 m^2g^{-1}) and average pore diameters (1.65−2.88 nm). Notably, B_2–pC exhibited high capacitance (312.3 F g^{-1}), ~98.5% capacitance retention after 2500 cycles and demonstrated high-rate capability up to 20 A g^{-1} as a supercapacitor electrode; due to the combined contribution of the EDL capacitance and pseudocapacitance. Compared with the undoped carbon (B_0–pC) electrode with fewer mesopores, the boron dopant in B_2–pC enhanced its specific capacitance due to the pseudocapacitive effect and its larger mesopores ensured better high-rate response. The regression analysis from the developed ANN model (high R^2=0.93–0.99 and low MSE=0.0089–0.0214) after 3400 epochs is suitable to model the electrode performance.

REFERENCES

[1] J. Tao *et al.*, "Solid-state high performance flexible supercapacitors based on polypyrrole-MnO2-carbon fiber hybrid structure.," *Sci. Rep.*, vol. 3, p. 2286, 2013, doi: 10.1038/srep02286.

[2] Y. Matsuda, K. Inoue, H. Takeuchi, and Y. Okuhama, "Gel polymer electrolytes for electric double layer capacitors," *Solid State Ionics*, vol. 113, pp. 103–107, 1998.

[3] R. Taniki, K. Matsumoto, T. Nohira, and R. Hagiwara, "All solid-state electrochemical capacitors using N, N-dimethylpyrrolidinium fluorohydrogenate as ionic plastic crystal electrolyte," *J. Power Sources*, vol. 245, pp. 758–763, 2014.

[4] P. Simon and Y. Gogotsi, "Materials for electrochemical capacitors," in *Nanoscience and technology: a collection of reviews from Nature journals*, World Scientific, 2010, pp. 320–329.

[5] X. Zheng, J. Luo, W. Lv, D. Wang, and Q. Yang, "Carbon: Two-Dimensional Porous Carbon: Synthesis and Ion-Transport Properties (Adv. Mater. 36/2015)," *Adv. Mater.*, vol. 27, no. 36, p. 5254, 2015.

[6] D. Ge *et al.*, "Foldable supercapacitors from triple networks of macroporous cellulose fibers, single-walled carbon nanotubes and polyaniline nanoribbons," *Nano Energy*, vol. 11, pp. 568–578, 2015.

[7] W. Liu, Y. Feng, X. Yan, J. Chen, and Q. Xue, "Superior micro-supercapacitors based on graphene quantum dots," *Adv. Funct. Mater.*, vol. 23, no. 33, pp. 4111–4122, 2013.

[8] E. Lim, C. Jo, and J. Lee, "A mini review of designed mesoporous materials for energy-storage applications: from electric double-layer capacitors to hybrid supercapacitors," *Nanoscale*, vol. 8, no. 15, pp. 7827–7833, 2016.

[9] T. Kim, G. Jung, S. Yoo, K. S. Suh, and R. S. Ruoff, "Activated graphene-based carbons as supercapacitor electrodes with macro-and mesopores," *ACS Nano*, vol. 7, no. 8, pp. 6899–6905, 2013.

[10] S. Wang, B. Hsia, C. Carraro, and R. Maboudian, "High-performance all solid-state micro-supercapacitor based on patterned photoresist-derived porous carbon electrodes and an ionogel electrolyte," *J. Mater. Chem. A*, vol. 2, no. 21, pp. 7997–8002, 2014.

[11] M. De Corato, M. Bernasconi, L. D'Alessio, O. Ori, M. V Putz, and G. Benedek, "Topological versus physical and chemical properties of negatively curved carbon surfaces," in *Topological Modelling of Nanostructures and Extended Systems*, Springer, 2013, pp. 105–136.

[12] G. Luo *et al.*, "Facile synthesis of porous graphene as binder-free electrode for supercapacitor application," *Appl. Surf. Sci.*, vol. 366, pp. 46–52, 2016.

[13] J. H. Kim, S. Lee, J. W. Lee, T. Song, and U. Paik, "3D-interconnected

nanoporous RGO-CNT structure for supercapacitors application," *Electrochim. Acta*, vol. 125, pp. 536–542, 2014.

[14] J. Chang *et al.*, "Activated porous carbon prepared from paulownia flower for high performance supercapacitor electrodes," *Electrochim. Acta*, vol. 157, pp. 290–298, 2015.

[15] G.-H. An, J. I. Sohn, and H.-J. Ahn, "Hierarchical architecture of hybrid carbon-encapsulated hollow manganese oxide nanotubes with a porous-wall structure for high-performance electrochemical energy storage," *J. Mater. Chem. A*, vol. 4, no. 6, pp. 2049–2054, 2016.

[16] M. Zhou, F. Pu, Z. Wang, and S. Guan, "Nitrogen-doped porous carbons through KOH activation with superior performance in supercapacitors," *Carbon N. Y.*, vol. 68, pp. 185–194, 2014.

[17] Z. Yang *et al.*, "Recent advancement of nanostructured carbon for energy applications," *Chem. Rev.*, vol. 115, no. 11, pp. 5159–5223, 2015.

[18] Z. Gao, Y. Zhang, N. Song, and X. Li, "Biomass-derived renewable carbon materials for electrochemical energy storage," *Mater. Res. Lett.*, vol. 5, no. 2, pp. 69–88, 2017.

[19] V. Subramanian, C. Luo, A. M. Stephan, K. S. Nahm, S. Thomas, and B. Wei, "Supercapacitors from activated carbon derived from banana fibers," *J. Phys. Chem. C*, vol. 111, no. 20, pp. 7527–7531, 2007.

[20] M. S. Balathanigaimani, W.-G. Shim, M.-J. Lee, C. Kim, J.-W. Lee, and H. Moon, "Highly porous electrodes from novel corn grains-based activated carbons for electrical double layer capacitors," *Electrochem. commun.*, vol. 10, no. 6, pp. 868–871, 2008.

[21] F.-C. Wu, R.-L. Tseng, C.-C. Hu, and C.-C. Wang, "Effects of pore structure and electrolyte on the capacitive characteristics of steam-and KOH-activated carbons for supercapacitors," *J. Power Sources*, vol. 144, no. 1, pp. 302–309, 2005.

[22] K. Konno, Y. Ohba, K. Onoe, and T. Yamaguchi, "Preparation of activated carbon having the structure derived from biomass by alkali activation with NaOH, and its application for electric double-layer capacitor," *Tanso*, vol. 2008, no. 231, pp. 2–7, 2008.

[23] L. Wei and G. Yushin, "Electrical double layer capacitors with sucrose derived carbon electrodes in ionic liquid electrolytes," *J. Power Sources*, vol. 196, no. 8, pp. 4072–4079, 2011.

[24] C. Zhong, Y. Deng, W. Hu, J. Qiao, L. Zhang, and J. Zhang, "A review of electrolyte materials and compositions for electrochemical supercapacitors," *Chem. Soc. Rev.*, vol. 44, no. 21, pp. 7484–7539, 2015.

[25] G. Wang, L. Zhang, and J. Zhang, "A review of electrode materials for electrochemical supercapacitors," *Chem. Soc. Rev.*, vol. 41, no. 2, pp. 797–828, 2012.

[26] J. P. Zheng, J. Huang, and T. R. Jow, "The limitations of energy density for electrochemical capacitors," *J. Electrochem. Soc.*, vol. 144, no. 6, p. 2026, 1997.

[27] V. Augustyn, P. Simon, and B. Dunn, "Pseudocapacitive oxide materials for high-rate electrochemical energy storage," *Energy Environ. Sci.*, vol. 7, no. 5, pp. 1597–1614, 2014.

[28] Y.-G. Wang, Z.-D. Wang, and Y.-Y. Xia, "An asymmetric supercapacitor using RuO2/TiO2 nanotube composite and activated carbon electrodes," *Electrochim. Acta*, vol. 50, no. 28, pp. 5641–5646, 2005.

[29] J. W. Long, D. Bélanger, T. Brousse, W. Sugimoto, M. B. Sassin, and O. Crosnier, "Asymmetric electrochemical capacitors-stretching the limits of aqueous electrolytes," NAVAL RESEARCH LAB WASHINGTON DC, 2011.

[30] M.-Y. Cho, M.-H. Kim, H.-K. Kim, K.-B. Kim, J. R. Yoon, and K. C. Roh, "Electrochemical performance of hybrid supercapacitor fabricated using multi-structured activated carbon," *Electrochem. commun.*, vol. 47, pp. 5–8, 2014.

[31] P. Perret, Z. Khani, T. Brousse, D. Bélanger, and D. Guay, "Carbon/PbO2 asymmetric electrochemical capacitor based on methanesulfonic acid electrolyte," *Electrochim. Acta*, vol. 56, no. 24, pp. 8122–8128, 2011.

[32] W. Shimizu, S. Makino, K. Takahashi, N. Imanishi, and W. Sugimoto, "Development of a 4.2 V aqueous hybrid electrochemical capacitor based on MnO2 positive and protected Li negative electrodes," *J. Power Sources*, vol. 241,

pp. 572–577, 2013.

[33] B. E. Conway, *Electrochemical supercapacitors: scientific fundamentals and technological applications*. Springer Science & Business Media, 2013.

[34] X. Zhao, B. M. Sánchez, P. J. Dobson, and P. S. Grant, "The role of nanomaterials in redox-based supercapacitors for next generation energy storage devices," *Nanoscale*, vol. 3, no. 3, pp. 839–855, 2011.

[35] V. I. Birss, B. E. Conway, and J. Wojtowicz, "The role and utilization of pseudocapacitance for energy storage by supercapacitors," 1997.

[36] J. Zhang and X. S. Zhao, "On the configuration of supercapacitors for maximizing electrochemical performance," *ChemSusChem*, vol. 5, no. 5, pp. 818–841, 2012.

[37] D. Hulicova-Jurcakova, A. M. Puziy, O. I. Poddubnaya, F. Suárez-García, J. M. D. Tascón, and G. Q. Lu, "Highly stable performance of supercapacitors from phosphorus-enriched carbons," *J. Am. Chem. Soc.*, vol. 131, no. 14, pp. 5026–5027, 2009.

[38] Z. Niu *et al.*, "Compact-designed supercapacitors using free-standing single-walled carbon nanotube films," *Energy Environ. Sci.*, vol. 4, no. 4, pp. 1440–1446, 2011.

[39] M. D. Stoller and R. S. Ruoff, "Best practice methods for determining an electrode material's performance for ultracapacitors," *Energy Environ. Sci.*, vol. 3, no. 9,

pp. 1294–1301, 2010.

[40] T. Chen *et al.*, "All-solid-state high performance asymmetric supercapacitors based on novel MnS nanocrystal and activated carbon materials," *Sci. Rep.*, vol. 6, p. 23289, 2016.

[41] K. Bhattacharya and P. Deb, "Hybrid nanostructured C-dot decorated Fe 3 O 4 electrode materials for superior electrochemical energy storage performance," *Dalt. Trans.*, vol. 44, no. 19, pp. 9221–9229, 2015.

[42] D. T. Pham *et al.*, "Carbon nanotube-bridged graphene 3D building blocks for ultrafast compact supercapacitors," *ACS Nano*, vol. 9, no. 2, pp. 2018–2027, 2015.

[43] L. Zhi *et al.*, "Hierarchical graphene network sandwiched by a thin carbon layer for capacitive energy storage," *Carbon N. Y.*, vol. 113, pp. 100–107, 2017.

[44] F. Zhang *et al.*, "Hierarchically porous carbon foams for electric double layer capacitors," *Nano Res.*, vol. 9, no. 10, pp. 2875–2888, 2016.

[45] T. Liu *et al.*, "Polyaniline and polypyrrole pseudocapacitor electrodes with excellent cycling stability," *Nano Lett.*, vol. 14, no. 5, pp. 2522–2527, 2014.

[46] H. Lu and X. S. Zhao, "Biomass-derived carbon electrode materials for supercapacitors," *Sustain. Energy Fuels*, vol. 1, no. 6, pp. 1265–1281, 2017.

[47] L. L. Zhang and X. S. Zhao, "Carbon-based materials as supercapacitor

electrodes," *Chem. Soc. Rev.*, vol. 38, no. 9, pp. 2520–2531, 2009.

[48] G. Wang *et al.*, "Solid-state supercapacitor based on activated carbon cloths exhibits excellent rate capability," *Adv. Mater.*, vol. 26, no. 17, pp. 2676–2682, 2014.

[49] Y. Li, S. Roy, T. Ben, S. Xu, and S. Qiu, "Micropore engineering of carbonized porous aromatic framework (PAF-1) for supercapacitors application," *Phys. Chem. Chem. Phys.*, vol. 16, no. 25, pp. 12909–12917, 2014.

[50] K. S. W. Sing, "Reporting physisorption data for gas/solid systems with special reference to the determination of surface area and porosity (Recommendations 1984)," *Pure Appl. Chem.*, vol. 57, no. 4, pp. 603–619, 1985.

[51] M. Thommes *et al.*, "Physisorption of gases, with special reference to the evaluation of surface area and pore size distribution (IUPAC Technical Report)," *Pure Appl. Chem.*, vol. 87, no. 9–10, pp. 1051–1069, 2015.

[52] M.-M. Titirici and M. Antonietti, "Chemistry and materials options of sustainable carbon materials made by hydrothermal carbonization," *Chem. Soc. Rev.*, vol. 39, no. 1, pp. 103–116, 2010.

[53] J. Wang and S. Kaskel, "KOH activation of carbon-based materials for energy storage," *J. Mater. Chem.*, vol. 22, no. 45, pp. 23710–23725, 2012.

[54] S. Dutta, A. Bhaumik, and K. C.-W. Wu, "Hierarchically porous carbon derived

from polymers and biomass: effect of interconnected pores on energy applications," *Energy Environ. Sci.*, vol. 7, no. 11, pp. 3574–3592, 2014.

[55] M.-M. Titirici, R. J. White, C. Falco, and M. Sevilla, "Black perspectives for a green future: hydrothermal carbons for environment protection and energy storage," *Energy Environ. Sci.*, vol. 5, no. 5, pp. 6796–6822, 2012.

[56] K. Shi, J. Yan, E. Lester, and T. Wu, "Catalyst-free synthesis of multiwalled carbon nanotubes via microwave-induced processing of biomass," *Ind. Eng. Chem. Res.*, vol. 53, no. 39, pp. 15012–15019, 2014.

[57] A. Demirbaş, "Biomass resource facilities and biomass conversion processing for fuels and chemicals," *Energy Convers. Manag.*, vol. 42, no. 11, pp. 1357–1378, 2001.

[58] A. C. Caputo, M. Palumbo, P. M. Pelagagge, and F. Scacchia, "Economics of biomass energy utilization in combustion and gasification plants: effects of logistic variables," *Biomass and Bioenergy*, vol. 28, no. 1, pp. 35–51, 2005.

[59] S. Kim and B. E. Dale, "Life cycle assessment of various cropping systems utilized for producing biofuels: bioethanol and biodiesel," *Biomass and Bioenergy*, vol. 29, no. 6, pp. 426–439, 2005.

[60] R. A. Sheldon, "Green and sustainable manufacture of chemicals from biomass: state of the art," *Green Chem.*, vol. 16, no. 3, pp. 950–963, 2014.

[61] C. J. Atkinson, J. D. Fitzgerald, and N. A. Hipps, "Potential mechanisms for achieving agricultural benefits from biochar application to temperate soils: a review," *Plant Soil*, vol. 337, no. 1–2, pp. 1–18, 2010.

[62] O. Ioannidou and A. Zabaniotou, "Agricultural residues as precursors for activated carbon production—a review," *Renew. Sustain. energy Rev.*, vol. 11, no. 9, pp. 1966–2005, 2007.

[63] S. Manocha, L. M. Manocha, P. Joshi, B. Patel, G. Dangi, and N. Verma, "Activated carbon from biomass," in *AIP conference proceedings*, 2013, vol. 1538, no. 1, pp. 120–123.

[64] P. McKendry, "Energy production from biomass (part 2): conversion technologies," *Bioresour. Technol.*, vol. 83, no. 1, pp. 47–54, 2002.

[65] A. E. Pütün, N. Özbay, E. P. Önal, and E. Pütün, "Fixed-bed pyrolysis of cotton stalk for liquid and solid products," *Fuel Process. Technol.*, vol. 86, no. 11, pp. 1207–1219, 2005.

[66] A. Primo, P. Atienzar, E. Sanchez, J. M. Delgado, and H. García, "From biomass wastes to large-area, high-quality, N-doped graphene: catalyst-free carbonization of chitosan coatings on arbitrary substrates," *Chem. Commun.*, vol. 48, no. 74, pp. 9254–9256, 2012.

[67] A. S. Marriott *et al.*, "Investigating the structure of biomass-derived non-graphitizing mesoporous carbons by electron energy loss spectroscopy in the

transmission electron microscope and X-ray photoelectron spectroscopy," *Carbon N. Y.*, vol. 67, pp. 514–524, 2014.

[68] A. Aworn, P. Thiravetyan, and W. Nakbanpote, "Preparation and characteristics of agricultural waste activated carbon by physical activation having micro- and mesopores," *J. Anal. Appl. Pyrolysis*, vol. 82, no. 2, pp. 279–285, 2008, doi: https://doi.org/10.1016/j.jaap.2008.04.007.

[69] D. S. Su, "The use of natural materials in nanocarbon synthesis," *ChemSusChem Chem. Sustain. Energy Mater.*, vol. 2, no. 11, pp. 1009–1020, 2009.

[70] D. S. Su and G. Centi, "A perspective on carbon materials for future energy application," *J. energy Chem.*, vol. 22, no. 2, pp. 151–173, 2013.

[71] A.-N. A. El-Hendawy, S. E. Samra, and B. S. Girgis, "Adsorption characteristics of activated carbons obtained from corncobs," *Colloids Surfaces A Physicochem. Eng. Asp.*, vol. 180, no. 3, pp. 209–221, 2001.

[72] F. Rodriguez-Reinoso and M. Molina-Sabio, "Activated carbons from lignocellulosic materials by chemical and/or physical activation: an overview," *Carbon N. Y.*, vol. 30, no. 7, pp. 1111–1118, 1992.

[73] T. Zhang, W. P. Walawender, L. T. Fan, M. Fan, D. Daugaard, and R. C. Brown, "Preparation of activated carbon from forest and agricultural residues through CO2 activation," *Chem. Eng. J.*, vol. 105, no. 1–2, pp. 53–59, 2004.

[74] A. A. M. Daifullah, S. M. Yakout, and S. A. Elreefy, "Adsorption of fluoride in aqueous solutions using KMnO4-modified activated carbon derived from steam pyrolysis of rice straw," *J. Hazard. Mater.*, vol. 147, no. 1, pp. 633–643, 2007, doi: https://doi.org/10.1016/j.jhazmat.2007.01.062.

[75] S. Balci, T. Doğu, and H. Yücel, "Characterization of activated carbon produced from almond shell and hazelnut shell," *J. Chem. Technol. Biotechnol.*, vol. 60, no. 4, pp. 419–426, Aug. 1994, doi: 10.1002/jctb.280600413.

[76] D. Prahas, Y. Kartika, N. Indraswati, and S. Ismadji, "Activated carbon from jackfruit peel waste by H3PO4 chemical activation: Pore structure and surface chemistry characterization," *Chem. Eng. J.*, vol. 140, no. 1, pp. 32–42, 2008, doi: https://doi.org/10.1016/j.cej.2007.08.032.

[77] F. Caturla, M. Molina-Sabio, and F. Rodríguez-Reinoso, "Preparation of activated carbon by chemical activation with ZnCl2," *Carbon N. Y.*, vol. 29, no. 7, pp. 999–1007, 1991, doi: https://doi.org/10.1016/0008-6223(91)90179-M.

[78] M. A. Lillo-Ródenas, D. Cazorla-Amorós, and A. Linares-Solano, "Understanding chemical reactions between carbons and NaOH and KOH: An insight into the chemical activation mechanism," *Carbon N. Y.*, vol. 41, no. 2, pp. 267–275, 2003, doi: https://doi.org/10.1016/S0008-6223(02)00279-8.

[79] J. Hayashi, T. Horikawa, I. Takeda, K. Muroyama, and F. Nasir Ani, "Preparing activated carbon from various nutshells by chemical activation with K2CO3," *Carbon N. Y.*, vol. 40, no. 13, pp. 2381–2386, 2002, doi:

https://doi.org/10.1016/S0008-6223(02)00118-5.

[80] T. Otowa, Y. Nojima, and T. Miyazaki, "Development of KOH activated high surface area carbon and its application to drinking water purification," *Carbon N. Y.*, vol. 35, no. 9, pp. 1315–1319, 1997, doi: https://doi.org/10.1016/S0008-6223(97)00076-6.

[81] Y. Juan and Q. Ke-qiang, "Preparation of Activated Carbon by Chemical Activation under Vacuum," *Environ. Sci. Technol.*, vol. 43, no. 9, pp. 3385–3390, May 2009, doi: 10.1021/es8036115.

[82] J. Hayashi, A. Kazehaya, K. Muroyama, and A. P. Watkinson, "Preparation of activated carbon from lignin by chemical activation," *Carbon N. Y.*, vol. 38, no. 13, pp. 1873–1878, 2000, doi: https://doi.org/10.1016/S0008-6223(00)00027-0.

[83] W. Huang, H. Zhang, Y. Huang, W. Wang, and S. Wei, "Hierarchical porous carbon obtained from animal bone and evaluation in electric double-layer capacitors," *Carbon N. Y.*, vol. 49, no. 3, pp. 838–843, 2011, doi: https://doi.org/10.1016/j.carbon.2010.10.025.

[84] X. Wu, L. Jiang, C. Long, and Z. Fan, "From flour to honeycomb-like carbon foam: Carbon makes room for high energy density supercapacitors," *Nano Energy*, vol. 13, pp. 527–536, 2015, doi: https://doi.org/10.1016/j.nanoen.2015.03.013.

[85] X. Li, C. Han, X. Chen, and C. Shi, "Preparation and performance of straw based activated carbon for supercapacitor in non-aqueous electrolytes," *Microporous*

Mesoporous Mater., vol. 131, no. 1, pp. 303–309, 2010, doi: https://doi.org/10.1016/j.micromeso.2010.01.007.

[86] W.-H. Qu, Y.-Y. Xu, A.-H. Lu, X.-Q. Zhang, and W.-C. Li, "Converting biowaste corncob residue into high value added porous carbon for supercapacitor electrodes," *Bioresour. Technol.*, vol. 189, pp. 285–291, 2015, doi: https://doi.org/10.1016/j.biortech.2015.04.005.

[87] H. Zhu, X. Wang, F. Yang, and X. Yang, "Promising Carbons for Supercapacitors Derived from Fungi," *Adv. Mater.*, vol. 23, no. 24, pp. 2745–2748, Jun. 2011, doi: 10.1002/adma.201100901.

[88] H. Wang, Z. Li, and D. Mitlin, "Tailoring Biomass-Derived Carbon Nanoarchitectures for High-Performance Supercapacitors," *ChemElectroChem*, vol. 1, no. 2, pp. 332–337, Feb. 2014, doi: 10.1002/celc.201300127.

[89] Q. Liang *et al.*, "A honeycomb-like porous carbon derived from pomelo peel for use in high-performance supercapacitors," *Nanoscale*, vol. 6, no. 22, pp. 13831–13837, 2014, doi: 10.1039/C4NR04541F.

[90] B. Xu, S. Hou, G. Cao, F. Wu, and Y. Yang, "Sustainable nitrogen-doped porous carbon with high surface areas prepared from gelatin for supercapacitors," *J. Mater. Chem.*, vol. 22, no. 36, pp. 19088–19093, 2012, doi: 10.1039/C2JM32759G.

[91] S. Zhao *et al.*, "A novel porous nanocomposite of sulfur/carbon obtained from

fish scales for lithium–sulfur batteries," *J. Mater. Chem. A*, vol. 1, no. 10, pp. 3334–3339, 2013, doi: 10.1039/C3TA01220D.

[92] E. Berl and A. Schmidt, "Über die Entstehung der Kohlen. II. Die Inkohlung von Cellulose und Lignin in neutralem Medium," *Justus Liebigs Ann. Chem.*, vol. 493, no. 1, pp. 97–123, Jan. 1932, doi: 10.1002/jlac.19324930106.

[93] B. Hu, K. Wang, L. Wu, S.-H. Yu, M. Antonietti, and M.-M. Titirici, "Engineering Carbon Materials from the Hydrothermal Carbonization Process of Biomass," *Adv. Mater.*, vol. 22, no. 7, pp. 813–828, Feb. 2010, doi: 10.1002/adma.200902812.

[94] M.-M. Titirici, M. Antonietti, and N. Baccile, "Hydrothermal carbon from biomass: a comparison of the local structure from poly- to monosaccharides and pentoses/hexoses," *Green Chem.*, vol. 10, no. 11, pp. 1204–1212, 2008, doi: 10.1039/B807009A.

[95] M. Sevilla, A. B. Fuertes, and R. Mokaya, "High density hydrogen storage in superactivated carbons from hydrothermally carbonized renewable organic materials," *Energy Environ. Sci.*, vol. 4, no. 4, pp. 1400–1410, 2011, doi: 10.1039/C0EE00347F.

[96] M.-M. Titirici, A. Thomas, and M. Antonietti, "Replication and Coating of Silica Templates by Hydrothermal Carbonization," *Adv. Funct. Mater.*, vol. 17, no. 6, pp. 1010–1018, Apr. 2007, doi: 10.1002/adfm.200600501.

[97] Z. Gao *et al.*, "Graphene Nanosheet/Ni2+/Al3+ Layered Double-Hydroxide Composite as a Novel Electrode for a Supercapacitor," *Chem. Mater.*, vol. 23, no. 15, pp. 3509–3516, Aug. 2011, doi: 10.1021/cm200975x.

[98] J. Wang *et al.*, "Green synthesis of graphene nanosheets/ZnO composites and electrochemical properties," *J. Solid State Chem.*, vol. 184, no. 6, pp. 1421–1427, 2011, doi: https://doi.org/10.1016/j.jssc.2011.03.006.

[99] W. Yang, Z. Gao, J. Ma, X. Zhang, and J. Wang, "Controlled synthesis of Co3O4 and Co3O4@MnO2 nanoarchitectures and their electrochemical capacitor application," *J. Alloys Compd.*, vol. 611, pp. 171–178, 2014, doi: https://doi.org/10.1016/j.jallcom.2014.04.085.

[100] Z. Gao *et al.*, "Synthesis and Exfoliation of Layered α-Co (OH) 2 Nanosheets and Their Electrochemical Performance for Supercapacitors," *Eur. J. Inorg. Chem.*, vol. 2013, no. 27, pp. 4832–4838, 2013.

[101] W. Yang, Z. Gao, N. Song, Y. Zhang, Y. Yang, and J. Wang, "Synthesis of hollow polyaniline nano-capsules and their supercapacitor application," *J. Power Sources*, vol. 272, pp. 915–921, 2014, doi: https://doi.org/10.1016/j.jpowsour.2014.09.013.

[102] D. A and G. Hegde, "Activated carbon nanospheres derived from bio-waste materials for supercapacitor applications – a review," *RSC Adv.*, vol. 5, no. 107, pp. 88339–88352, 2015, doi: 10.1039/C5RA19392C.

[103] M. Zhi, F. Yang, F. Meng, M. Li, A. Manivannan, and N. Wu, "Effects of Pore Structure on Performance of An Activated-Carbon Supercapacitor Electrode Recycled from Scrap Waste Tires," *ACS Sustain. Chem. Eng.*, vol. 2, no. 7, pp. 1592–1598, Jul. 2014, doi: 10.1021/sc500336h.

[104] A. M. Abioye and F. N. Ani, "Recent development in the production of activated carbon electrodes from agricultural waste biomass for supercapacitors: A review," *Renew. Sustain. Energy Rev.*, vol. 52, pp. 1282–1293, 2015, doi: https://doi.org/10.1016/j.rser.2015.07.129.

[105] J. Zhou, M. Wang, and X. Li, "Facile preparation of nitrogen-doped high-surface-area porous carbon derived from sucrose for high performance supercapacitors," *Appl. Surf. Sci.*, vol. 462, pp. 444–452, 2018, doi: https://doi.org/10.1016/j.apsusc.2018.08.158.

[106] P. Guo, Y. Gu, Z. Lei, Y. Cui, and X. S. Zhao, "Preparation of sucrose-based microporous carbons and their application as electrode materials for supercapacitors," *Microporous Mesoporous Mater.*, vol. 156, pp. 176–180, 2012, doi: https://doi.org/10.1016/j.micromeso.2012.02.043.

[107] H.-M. Luo, Y.-F. Yang, Y.-X. Sun, X. Zhao, and J.-Q. Zhang, "Preparation of fructose-based attapulgite template carbon materials and their electrochemical performance as supercapacitor electrodes," *J. Solid State Electrochem.*, vol. 19, no. 5, pp. 1491–1500, 2015, doi: 10.1007/s10008-015-2763-5.

[108] N. Subramanian and B. Viswanathan, "Nitrogen- and oxygen-containing

activated carbons from sucrose for electrochemical supercapacitor applications," *RSC Adv.*, vol. 5, no. 77, pp. 63000–63011, 2015, doi: 10.1039/C5RA06661A.

[109] L. Zhao *et al.*, "Nitrogen-Containing Hydrothermal Carbons with Superior Performance in Supercapacitors," *Adv. Mater.*, vol. 22, no. 45, pp. 5202–5206, Dec. 2010, doi: 10.1002/adma.201002647.

[110] J. M. Valente Nabais, J. G. Teixeira, and I. Almeida, "Development of easy made low cost bindless monolithic electrodes from biomass with controlled properties to be used as electrochemical capacitors," *Bioresour. Technol.*, vol. 102, no. 3, pp. 2781–2787, 2011, doi: https://doi.org/10.1016/j.biortech.2010.11.083.

[111] E. Taer, "Preparation of a highly porous," *Int. J. Electrochem. Sci*, vol. 6, pp. 3301–3315, 2011.

[112] D. Kalpana, S. H. Cho, S. B. Lee, Y. S. Lee, R. Misra, and N. G. Renganathan, "Recycled waste paper—A new source of raw material for electric double-layer capacitors," *J. Power Sources*, vol. 190, no. 2, pp. 587–591, 2009, doi: https://doi.org/10.1016/j.jpowsour.2009.01.058.

[113] Y.-T. Li, Y.-T. Pi, L.-M. Lu, S.-H. Xu, and T.-Z. Ren, "Hierarchical porous active carbon from fallen leaves by synergy of K2CO3 and their supercapacitor performance," *J. Power Sources*, vol. 299, pp. 519–528, 2015, doi: https://doi.org/10.1016/j.jpowsour.2015.09.039.

[114] C. Peng, X. Yan, R. Wang, J. Lang, Y. Ou, and Q. Xue, "Promising activated

carbons derived from waste tea-leaves and their application in high performance supercapacitors electrodes," *Electrochim. Acta*, vol. 87, pp. 401–408, 2013, doi: https://doi.org/10.1016/j.electacta.2012.09.082.

[115] X. Li *et al.*, "Preparation of capacitor's electrode from sunflower seed shell," *Bioresour. Technol.*, vol. 102, no. 2, pp. 1118–1123, 2011, doi: https://doi.org/10.1016/j.biortech.2010.08.110.

[116] J. Hou, C. Cao, F. Idrees, and X. Ma, "Hierarchical Porous Nitrogen-Doped Carbon Nanosheets Derived from Silk for Ultrahigh-Capacity Battery Anodes and Supercapacitors," *ACS Nano*, vol. 9, no. 3, pp. 2556–2564, Mar. 2015, doi: 10.1021/nn506394r.

[117] H. Feng *et al.*, "Three-dimensional honeycomb-like hierarchically structured carbon for high-performance supercapacitors derived from high-ash-content sewage sludge," *J. Mater. Chem. A*, vol. 3, no. 29, pp. 15225–15234, 2015, doi: 10.1039/C5TA03217B.

[118] W. Chen, H. Zhang, Y. Huang, and W. Wang, "A fish scale based hierarchical lamellar porous carbon material obtained using a natural template for high performance electrochemical capacitors," *J. Mater. Chem.*, vol. 20, no. 23, pp. 4773–4775, 2010, doi: 10.1039/C0JM00382D.

[119] M. Olivares-Marín *et al.*, "Cherry stones as precursor of activated carbons for supercapacitors," *Mater. Chem. Phys.*, vol. 114, no. 1, pp. 323–327, 2009, doi: https://doi.org/10.1016/j.matchemphys.2008.09.010.

[120]   J. Li and Q. Wu, "Water bamboo-derived porous carbons as electrode materials for supercapacitors," *New J. Chem.*, vol. 39, no. 5, pp. 3859–3864, 2015, doi: 10.1039/C4NJ01853B.

[121]   H. Sun, W. He, C. Zong, and L. Lu, "Template-Free Synthesis of Renewable Macroporous Carbon via Yeast Cells for High-Performance Supercapacitor Electrode Materials," *ACS Appl. Mater. Interfaces*, vol. 5, no. 6, pp. 2261–2268, Mar. 2013, doi: 10.1021/am400206r.

[122]   K. Karthikeyan *et al.*, "Construction of High-Energy-Density Supercapacitors from Pine-Cone-Derived High-Surface-Area Carbons," *ChemSusChem*, vol. 7, no. 5, pp. 1435–1442, May 2014, doi: 10.1002/cssc.201301262.

[123]   R. Wang, P. Wang, X. Yan, J. Lang, C. Peng, and Q. Xue, "Promising Porous Carbon Derived from Celtuce Leaves with Outstanding Supercapacitance and CO2 Capture Performance," *ACS Appl. Mater. Interfaces*, vol. 4, no. 11, pp. 5800–5806, Nov. 2012, doi: 10.1021/am302077c.

[124]   L. Jiang, J. Yan, L. Hao, R. Xue, G. Sun, and B. Yi, "High rate performance activated carbons prepared from ginkgo shells for electrochemical supercapacitors," *Carbon N. Y.*, vol. 56, pp. 146–154, 2013, doi: https://doi.org/10.1016/j.carbon.2012.12.085.

[125] W. Qian *et al.*, "Human hair-derived carbon flakes for electrochemical supercapacitors," *Energy Environ. Sci.*, vol. 7, no. 1, pp. 379–386, 2014, doi: 10.1039/C3EE43111H.

[126] C. Falco *et al.*, "Hydrothermal carbons from hemicellulose-derived aqueous hydrolysis products as electrode materials for supercapacitors," 2013.

[127] C. Long, X. Chen, L. Jiang, L. Zhi, and Z. Fan, "Porous layer-stacking carbon derived from in-built template in biomass for high volumetric performance supercapacitors," *Nano Energy*, vol. 12, pp. 141–151, 2015, doi: https://doi.org/10.1016/j.nanoen.2014.12.014.

[128] M. Sevilla, W. Gu, C. Falco, M. M. Titirici, A. B. Fuertes, and G. Yushin, "Hydrothermal synthesis of microalgae-derived microporous carbons for electrochemical capacitors," *J. Power Sources*, vol. 267, pp. 26–32, 2014, doi: https://doi.org/10.1016/j.jpowsour.2014.05.046.

[129] H. Wang *et al.*, "Interconnected Carbon Nanosheets Derived from Hemp for Ultrafast Supercapacitors with High Energy," *ACS Nano*, vol. 7, no. 6, pp. 5131–5141, Jun. 2013, doi: 10.1021/nn400731g.

[130] W. Tian *et al.*, "Bio-inspired beehive-like hierarchical nanoporous carbon derived from bamboo-based industrial by-product as a high performance supercapacitor electrode material," *J. Mater. Chem. A*, vol. 3, no. 10, pp. 5656–5664, 2015, doi: 10.1039/C4TA06620K.

[131] X.-L. Wu, T. Wen, H.-L. Guo, S. Yang, X. Wang, and A.-W. Xu, "Biomass-Derived Sponge-like Carbonaceous Hydrogels and Aerogels for Supercapacitors," *ACS Nano*, vol. 7, no. 4, pp. 3589–3597, Apr. 2013, doi: 10.1021/nn400566d.

[132] E. Frackowiak, G. Lota, J. Machnikowski, C. Vix-Guterl, and F. Béguin, "Optimisation of supercapacitors using carbons with controlled nanotexture and nitrogen content," *Electrochim. Acta*, vol. 51, no. 11, pp. 2209–2214, 2006, doi: https://doi.org/10.1016/j.electacta.2005.04.080.

[133] G. Lota, B. Grzyb, H. Machnikowska, J. Machnikowski, and E. Frackowiak, "Effect of nitrogen in carbon electrode on the supercapacitor performance," *Chem. Phys. Lett.*, vol. 404, no. 1, pp. 53–58, 2005, doi: https://doi.org/10.1016/j.cplett.2005.01.074.

[134] Y.-H. Lee, Y.-F. Lee, K.-H. Chang, and C.-C. Hu, "Synthesis of N-doped carbon nanosheets from collagen for electrochemical energy storage/conversion systems," *Electrochem. commun.*, vol. 13, no. 1, pp. 50–53, 2011, doi: https://doi.org/10.1016/j.elecom.2010.11.010.

[135] C. Qin, X. Lu, G. Yin, Z. Jin, Q. Tan, and X. Bai, "Study of activated nitrogen-enriched carbon and nitrogen-enriched carbon/carbon aerogel composite as cathode materials for supercapacitors," *Mater. Chem. Phys.*, vol. 126, no. 1, pp. 453–458, 2011, doi: https://doi.org/10.1016/j.matchemphys.2010.09.019.

[136] H. M. Jeong *et al.*, "Nitrogen-Doped Graphene for High-Performance Ultracapacitors and the Importance of Nitrogen-Doped Sites at Basal Planes," *Nano Lett.*, vol. 11, no. 6, pp. 2472–2477, Jun. 2011, doi: 10.1021/nl2009058.

[137] E. Raymundo-Piñero, F. Leroux, and F. Béguin, "A High-Performance Carbon for Supercapacitors Obtained by Carbonization of a Seaweed Biopolymer," *Adv.*

Mater., vol. 18, no. 14, pp. 1877–1882, Jul. 2006, doi: 10.1002/adma.200501905.

[138] E. Raymundo-Piñero, M. Cadek, and F. Béguin, "Tuning Carbon Materials for Supercapacitors by Direct Pyrolysis of Seaweeds," *Adv. Funct. Mater.*, vol. 19, no. 7, pp. 1032–1039, Apr. 2009, doi: 10.1002/adfm.200801057.

[139] E. Frackowiak, K. Metenier, V. Bertagna, and F. Beguin, "Supercapacitor electrodes from multiwalled carbon nanotubes," *Appl. Phys. Lett.*, vol. 77, no. 15, pp. 2421–2423, Oct. 2000, doi: 10.1063/1.1290146.

[140] C. O. Ania, V. Khomenko, E. Raymundo-Piñero, J. B. Parra, and F. Béguin, "The Large Electrochemical Capacitance of Microporous Doped Carbon Obtained by Using a Zeolite Template," *Adv. Funct. Mater.*, vol. 17, no. 11, pp. 1828–1836, Jul. 2007, doi: 10.1002/adfm.200600961.

[141] K. Jurewicz, K. Babeł, A. Źiółkowski, and H. Wachowska, "Ammoxidation of active carbons for improvement of supercapacitor characteristics," *Electrochim. Acta*, vol. 48, no. 11, pp. 1491–1498, 2003, doi: https://doi.org/10.1016/S0013-4686(03)00035-5.

[142] G. Lota, K. Fic, and E. Frackowiak, "Carbon nanotubes and their composites in electrochemical applications," *Energy Environ. Sci.*, vol. 4, no. 5, pp. 1592–1605, 2011, doi: 10.1039/C0EE00470G.

[143] L. R. Radovic, C. Moreno-Castilla, and J. Rivera-Utrilla, "Carbon materials as adsorbents in aqueous solutions," *Chem. Phys. carbon*, pp. 227–406, 2001.

[144] H. Chen *et al.*, "Boron and nitrogen co-doped porous carbon with a high concentration of boron and its superior capacitive behavior," *Carbon N. Y.*, vol. 113, pp. 266–273, 2017.

[145] F. Sun *et al.*, "In Situ Doping Boron Atoms into Porous Carbon Nanoparticles with Increased Oxygen Graft Enhances both Affinity and Durability toward Electrolyte for Greatly Improved Supercapacitive Performance," *Adv. Funct. Mater.*, vol. 28, no. 41, p. 1804190, Oct. 2018, doi: 10.1002/adfm.201804190.

[146] T. Ishii, T. Maie, N. Kimura, Y. Kobori, Y. Imashiro, and J. Ozaki, "Enhanced catalytic activity of nanoshell carbon co-doped with boron and nitrogen in the oxygen reduction reaction," *Int. J. Hydrogen Energy*, vol. 42, no. 23, pp. 15489–15496, 2017, doi: https://doi.org/10.1016/j.ijhydene.2017.05.003.

[147] D.-C. Guo *et al.*, "Ionic liquid C16mimBF4 assisted synthesis of poly(benzoxazine-co-resol)-based hierarchically porous carbons with superior performance in supercapacitors," *Energy Environ. Sci.*, vol. 6, no. 2, pp. 652–659, 2013, doi: 10.1039/C2EE23127A.

[148] X. Y. Chen, D. H. Xie, Z. J. Zhang, and C. Chen, "Tetraphenylborate-derived hierarchically porous carbons as efficient electrode materials for supercapacitors," *J. Power Sources*, vol. 246, pp. 531–539, 2014, doi: https://doi.org/10.1016/j.jpowsour.2013.08.013.

[149] H. Wu, W. Yuan, Y. Zhao, D. Han, X. Yuan, and L. Cheng, "B, N-dual doped sisal-based multiscale porous carbon for high-rate supercapacitors," *RSC Adv.*,

vol. 9, no. 3, pp. 1476–1486, 2019, doi: 10.1039/C8RA09663E.

[150] J. Hao, J. Wang, S. Qin, D. Liu, Y. Li, and W. Lei, "B/N co-doped carbon nanosphere frameworks as high-performance electrodes for supercapacitors," *J. Mater. Chem. A*, vol. 6, no. 17, pp. 8053–8058, 2018, doi: 10.1039/C8TA00683K.

[151] M. Sahoo, K. P. Sreena, B. P. Vinayan, and S. Ramaprabhu, "Green synthesis of boron doped graphene and its application as high performance anode material in Li ion battery," *Mater. Res. Bull.*, vol. 61, pp. 383–390, 2015, doi: https://doi.org/10.1016/j.materresbull.2014.10.049.

[152] R. Jain, R. Mehrotra, and S. Mishra, "Synthesis of B doped graphene/polyaniline hybrids for high-performance supercapacitor application," *J. Mater. Sci. Mater. Electron.*, vol. 30, no. 3, pp. 2316–2326, 2019, doi: 10.1007/s10854-018-0504-0.

[153] Z. Ling *et al.*, "Sustainable Synthesis and Assembly of Biomass-Derived B/N Co-Doped Carbon Nanosheets with Ultrahigh Aspect Ratio for High-Performance Supercapacitors," *Adv. Funct. Mater.*, vol. 26, no. 1, pp. 111–119, Jan. 2016, doi: 10.1002/adfm.201504004.

[154] V. Srinivasan, "Mathematical Modeling of Electrochemical Capacitors," *J. Electrochem. Soc.*, vol. 146, no. 5, p. 1650, 1999, doi: 10.1149/1.1391821.

[155] C. Lin, B. N. Popov, and H. J. Ploehn, "Modeling the Effects of Electrode Composition and Pore Structure on the Performance of Electrochemical

Capacitors," *J. Electrochem. Soc.*, vol. 149, no. 2, p. A167, 2002, doi: 10.1149/1.1431575.

[156]   S. Zhu *et al.*, "Artificial neural network enabled capacitance prediction for carbon-based supercapacitors," *Mater. Lett.*, vol. 233, pp. 294–297, 2018, doi: https://doi.org/10.1016/j.matlet.2018.09.028.

[157]   L. Saad Saoud and A. Khellaf, "A neural network based on an inexpensive eight-bit microcontroller," *Neural Comput. Appl.*, vol. 20, no. 3, pp. 329–334, 2011, doi: 10.1007/s00521-010-0377-5.

[158]   I. Turkoglu, "Hardware implementation of varicap diode's ANN model using PIC microcontrollers," *Sensors Actuators A Phys.*, vol. 138, no. 2, pp. 288–293, 2007, doi: https://doi.org/10.1016/j.sna.2007.05.003.

[159]   R. Bayindir, S. Sagiroglu, and I. Colak, "An intelligent power factor corrector for power system using artificial neural networks," *Electr. Power Syst. Res.*, vol. 79, no. 1, pp. 152–160, 2009, doi: https://doi.org/10.1016/j.epsr.2008.05.009.

[160]   J.-N. Marie-Francoise, H. Gualous, and A. Berthon, "Supercapacitor thermal- and electrical-behaviour modelling using ANN," *IEE Proceedings-Electric Power Appl.*, vol. 153, no. 2, pp. 255–262, 2006.

[161]   C. H. Wu, Y. H. Hung, and C. W. Hong, "On-line supercapacitor dynamic models for energy conversion and management," *Energy Convers. Manag.*, vol. 53, no. 1, pp. 337–345, 2012, doi:

https://doi.org/10.1016/j.enconman.2011.01.018.

[162] J. Wang, Z. Li, S. Yan, X. Yu, Y. Ma, and L. Ma, "Modifying the microstructure of algae-based active carbon and modelling supercapacitors using artificial neural networks," *RSC Adv.*, vol. 9, no. 26, pp. 14797–14808, 2019, doi: 10.1039/C9RA01255A.

[163] A. A. Oladipo, R. Vaziri, and M. A. Abureesh, "Highly robust AgIO3/MIL-53 (Fe) nanohybrid composites for degradation of organophosphorus pesticides in single and binary systems: Application of artificial neural networks modelling," *J. Taiwan Inst. Chem. Eng.*, vol. 83, pp. 133–142, 2018, doi: https://doi.org/10.1016/j.jtice.2017.12.013.

[164] A. A. Oladipo, M. A. Abureesh, and M. Gazi, "Bifunctional composite from spent 'Cyprus coffee' for tetracycline removal and phenol degradation: Solar-Fenton process and artificial neural network," *Int. J. Biol. Macromol.*, vol. 90, pp. 89–99, 2016, doi: https://doi.org/10.1016/j.ijbiomac.2015.08.054.

[165] A. S. Oladipo *et al.*, "Magnetic recyclable eggshell-based mesoporous catalyst for biodiesel production from crude neem oil: Process optimization by central composite design and artificial neural network," *Comptes Rendus Chim.*, vol. 21, no. 7, pp. 684–695, 2018, doi: https://doi.org/10.1016/j.crci.2018.03.011.

[166] T. D. Dongale, P. R. Jadhav, G. J. Navathe, J. H. Kim, M. M. Karanjkar, and P. S. Patil, "Development of nano fiber MnO2 thin film electrode and cyclic voltammetry behavior modeling using artificial neural network for supercapacitor

application," *Mater. Sci. Semicond. Process.*, vol. 36, pp. 43–48, 2015, doi: https://doi.org/10.1016/j.mssp.2015.02.084.

[167] S. L. Azarmi, A. A. Oladipo, R. Vaziri, and H. Alipour, "Comparative Modelling and Artificial Neural Network Inspired Prediction of Waste Generation Rates of Hospitality Industry: The Case of North Cyprus," *Sustainability* , vol. 10, no. 9. 2018, doi: 10.3390/su10092965.

[168] Y. Zhao, C. Zhang, Y. Zhang, Z. Wang, and J. Li, "A review of data mining technologies in building energy systems: Load prediction, pattern identification, fault detection and diagnosis," *Energy Built Environ.*, vol. 1, no. 2, pp. 149–164, 2020, doi: https://doi.org/10.1016/j.enbenv.2019.11.003.

[169] X. He *et al.*, "Flexible binder-free hierarchical copper sulfide/carbon cloth hybrid supercapacitor electrodes and the application as negative electrodes in asymmetric supercapacitor," *J. Mater. Sci. Mater. Electron.*, vol. 31, no. 3, pp. 2145–2152, 2020.

[170] M. Gazi, A. A. Oladipo, Z. E. Ojoro, and H. O. Gulcan, "High-performance nanocatalyst for adsorptive and photo-assisted Fenton-like degradation of phenol: modeling using artificial neural networks," *Chem. Eng. Commun.*, vol. 204, no. 7, pp. 729–738, 2017.

[171] Z. Shang *et al.*, "Houttuynia-derived nitrogen-doped hierarchically porous carbon for high-performance supercapacitor," *Carbon N. Y.*, vol. 161, pp. 62–70, 2020.

[172] A. A. Oladipo, E. O. Ahaka, and M. Gazi, "High adsorptive potential of calcined magnetic biochar derived from banana peels for Cu 2+, Hg 2+, and Zn 2+ ions removal in single and ternary systems," *Environ. Sci. Pollut. Res.*, vol. 26, no. 31, pp. 31887–31899, 2019.

[173] A. O. Ifebajo, A. A. Oladipo, and M. Gazi, "Efficient removal of tetracycline by CoO/CuFe 2 O 4 derived from layered double hydroxides," *Environ. Chem. Lett.*, vol. 17, no. 1, pp. 487–494, 2019.

[174] K. Yan *et al.*, "An asymmetric supercapacitor based on NiCo 2 O 4 nanosheets as anode and partially reduced graphene oxides/carbon nanotubes as cathode," *Chem. Pap.*, vol. 74, no. 2, pp. 591–599, 2020.

[175] M. Wang, J. Zhang, X. Yi, B. Liu, X. Zhao, and X. Liu, "High-performance asymmetric supercapacitor made of NiMoO4 nanorods@ Co3O4 on a cellulose-based carbon aerogel," *Beilstein J. Nanotechnol.*, vol. 11, no. 1, pp. 240–251, 2020.

[176] J. Li, X. Li, D. Xiong, L. Wang, and D. Li, "Enhanced capacitance of boron-doped graphene aerogels for aqueous symmetric supercapacitors," *Appl. Surf. Sci.*, vol. 475, pp. 285–293, 2019.

[177] J. Feng, W. Song, L. Sun, and L. Xu, "One-step nanocasting synthesis of nitrogen and phosphorus dual heteroatom doped ordered mesoporous carbons for supercapacitor application," *RSC Adv.*, vol. 6, no. 111, pp. 110337–110343, 2016.

[178] H. Guo and Q. Gao, "Boron and nitrogen co-doped porous carbon and its enhanced properties as supercapacitor," *J. Power Sources*, vol. 186, no. 2, pp. 551–556, 2009.

[179] Y. Ma *et al.*, "B/P/N/O co-doped hierarchical porous carbon nanofiber self-standing film with high volumetric and gravimetric capacitance performances for aqueous supercapacitors," *Electrochim. Acta*, vol. 337, p. 135800, 2020.

[180] E. G. Calvo, F. Lufrano, P. Staiti, A. Brigandì, A. Arenillas, and J. A. Menéndez, "Optimizing the electrochemical performance of aqueous symmetric supercapacitors based on an activated carbon xerogel," *J. Power Sources*, vol. 241, pp. 776–782, 2013.

[181] L. Bai, Y. Ge, and L. Bai, "Boron and Nitrogen co-doped porous carbons synthesized from polybenzoxazines for high-performance supercapacitors," *Coatings*, vol. 9, no. 10, p. 657, 2019.

[182] B.-A. Mei, O. Munteshari, J. Lau, B. Dunn, and L. Pilon, "Physical interpretations of Nyquist plots for EDLC electrodes and devices," *J. Phys. Chem. C*, vol. 122, no. 1, pp. 194–206, 2018.

[183] B. Amutha and M. Sathish, "A 2 V asymmetric supercapacitor based on reduced graphene oxide-carbon nanofiber-manganese carbonate nanocomposite and reduced graphene oxide in aqueous solution," *J. Solid State Electrochem.*, vol. 19, no. 8, pp. 2311–2320, 2015.

[184]   B. Pandit, D. P. Dubal, and B. R. Sankapal, "Large scale flexible solid state symmetric supercapacitor through inexpensive solution processed V2O5 complex surface architecture," *Electrochim. Acta*, vol. 242, pp. 382–389, 2017.

[185]   L. Tang, Y. Zhou, X. Zhou, Y. Chai, Q. Zheng, and D. Lin, "Enhancement in electrochemical performance of nitrogen-doped hierarchical porous carbon-based supercapacitor by optimizing activation temperature," *J. Mater. Sci. Mater. Electron.*, vol. 30, no. 3, pp. 2600–2609, 2019.

[186]   A. Cuña, E. L. da Silva, C. F. Malfatti, G. R. Gonçalves, M. A. Schettino, and J. C. C. Freitas, "Porous Carbon-Based Nanocomposites Containing Fe 2 P Nanoparticles as Promising Materials for Supercapacitor Electrodes," *J. Electron. Mater.*, vol. 49, no. 2, pp. 1059–1074, 2020.

[187]   E. Frackowiak and F. Béguin, "Supercapacitors: Materials, Systems and Applications," *Pozn. Wiley-VCH Verlag GmbH Co*, 2013.

[188]   Q. Gao, "Optimizing carbon/carbon supercapacitors in aqueous alkali sulfates electrolytes," *J. Energy Chem.*, vol. 38, pp. 219–224, 2019.